



# A theory for the response of tropical moist convection to mechanical orographic forcing

Quentin Nicolas\*

*Department of Earth and Planetary Science, University of California, Berkeley, California*

William R. Boos

*Department of Earth and Planetary Science, University of California, Berkeley, California*

*Climate and Ecosystem Sciences Division, Lawrence Berkeley National Laboratory, Berkeley, California*

\*Corresponding author: Quentin Nicolas, qnicolas@berkeley.edu

**Early Online Release:** This preliminary version has been accepted for publication in *Journal of the Atmospheric Sciences*, may be fully cited, and has been assigned DOI 10.1175/JAS-D-21-0218.1. The final typeset copyedited article will replace the EOR at the above DOI when it is published.

## ABSTRACT

Spatial patterns of tropical rainfall are strongly influenced by mountains. Although theories for precipitation induced by convectively stable upslope ascent exist for the midlatitudes, these do not represent the interaction of moist convection with orographic forcing. Here, we present a theory for convective precipitation produced by the mechanical interaction of a tropical ridge with a basic state horizontal wind. Deviations from this basic state are represented as the sum of a ‘dry’ perturbation, due to the stationary orographic gravity wave, and a ‘moist’ perturbation that carries the convective response. The moist component dynamics are subject to the weak temperature gradient approximation; they are forced by the dry mode’s influence on lower-tropospheric moisture and temperature. Analytical solutions provide estimates of the precipitation profile, including peak precipitation, upstream extent, and rain shadow extent. The theory can be used with several degrees of complexity depending on the technique used to compute the dry mode, which can be drawn from linear mountain wave theory or full numerical simulations. To evaluate the theory, we use a set of convection-permitting simulations with a flow-perpendicular ridge in a long channel. The theory makes a good prediction for the cross-slope precipitation profile, indicating that the organization of convective rain by orography can be quantitatively understood by considering the effect of stationary orographic gravity waves on a lower-tropospheric convective quasiequilibrium state.

## 1. Introduction

The spatial distribution of time-mean low-latitude rainfall is set to first order by the latitude and intensity of the intertropical convergence zone (ITCZ). Zonal inhomogeneities in sea-surface temperatures, a direct consequence of the presence of land masses, modify this distribution by driving the Walker circulation. These land masses also act seasonally as strong energy sources that drive monsoon circulations. On sufficiently large length scales, one might be satisfied with this description of the principal features and forcings of tropical precipitation; looking in more detail, however, one sees that orography strongly modifies these broad patterns.

Satellite-derived estimates (GPM IMERG V06B, Huffman et al. 2019) of climatological precipitation<sup>1</sup> for June-August and October-December are shown in Figure 1a,b, along with a smoothed contour of 500 m surface height. Some of the most striking deviations from the quasi-linear oceanic ITCZ are regions of intense rainfall located in the vicinity of mountains, e.g. near the Northern Andes, Western Ghats, Himalayas, and various ranges in the Indochinese peninsula and Maritime continent. These precipitation maxima are located in regions and seasons favorable to moist convective development, as noted by Xie et al. (2006) for the Asian summer monsoon and Ramesh et al. (2021) for regions experiencing an autumn monsoon. Xie et al. (2006) note that despite their prominence, a regional atmospheric model with 0.5° horizontal resolution is unable to reproduce these features. This failure, partly attributed to inadequate convective parameterization, was confirmed in a more systematic study by Kirshbaum (2020). It suggests that a main tool for evaluating climate, namely global circulation models, is ill-suited to study orographic convection, despite its importance for tropical precipitation.

---

<sup>1</sup>This GPM product has been shown to have little bias relative to rain gauge measurements on seasonal time scales, even over complex terrain (Derin et al. 2019).

Kirshbaum et al. (2018) identify two ways orography generates or alters convective systems: mechanical forcing, whereby a mountain lifts a background wind, and thermal forcing, where surface heat fluxes from elevated terrain produce convergence. Figure 1 displays 100 m wind vectors from the ERA5 reanalysis (Hersbach et al. 2020). Enhanced precipitation is mostly focused upwind of mountain ranges and on their windward slopes, suggesting that mechanical forcing is the primary mechanism at play in the large-scale, climatological sense. To further illustrate this point, we plot cross-sections of surface elevation and precipitation for summer and autumn along a latitude line spanning India, Southeast Asia, and the Philippines. We observe a clear shift of rainfall maxima from the western slopes in summer to the eastern slopes in autumn, consistent with the seasonal wind reversal in these regions.

Orographic precipitation in midlatitude, convectively stable flows has been extensively studied (for a review, see e.g. Roe 2005). Smith and Barstad (2004; hereafter SB04) developed an analytical theory, using linear mountain wave dynamics, that efficiently reproduces rainfall rates and spatial organization in such cases. It accounts for the effects of cloud latent heating through use of a moist stability parameter. However, because it does not account for moist convective dynamics, this theory may not be applicable to most tropical cases.

Orographic convection has been the focus of field experiments and numerous studies in the past two decades (Houze 2012; Kirshbaum et al. 2018). However, most have focused on synoptic scales, with little attention devoted to understanding what sets climatological time-mean precipitation rates. Chu and Lin (2000) and Chen and Lin (2005) studied initial value problems, where the fate of conditionally unstable flow was qualitatively examined as a function of moist nondimensional mountain height and convective available potential energy (CAPE). Miglietta and Rotunno (2009) extended their work to study the dependence on a more exhaustive set of parameters, noting that precipitation increased both with the ratio of mountain height to the level of free convection,

and with the aspect ratio of the mountain. The ratio of advective to convective time scales was shown to control the shape of the cross-mountain rainfall profile, with wider mountains having their precipitation profile shifted upstream. Subsequent studies (Miglietta and Rotunno 2012, 2014) noted the importance of vertical wind shear in producing large rain rates in the presence of deep convection; soundings with strong flow at lower levels and weak flow aloft produced higher precipitation rates. Focusing on larger spatial and temporal scales, Wang and Sobel (2017) simulated rainfall over isolated tropical islands in both thermally and mechanically forced settings. Their flat-island cases showed that surface roughness gradients alone can produce substantial mechanical forcing for precipitation, and that the transition from thermal to mechanical forcing can cause a non-monotonic dependence of mean precipitation on upstream wind speed.

Few studies attempted to formulate theories for orographically forced moist convection. Kirschbaum and Smith (2009) took inspiration from trade-wind flows over Dominica to develop an analytical model for the orographic enhancement of precipitation from shallow convection. They used a ‘slice’ method separating saturated updrafts from unsaturated descending air, computing the impact of an imposed mean ascent on vertical velocities. Two elements hamper application of this theory to the time-mean effects of orography on deep convection. First, the mean ascent is assumed to be uniform in height, whereas deep convection spans at least one vertical wavelength of an orographic gravity wave. Second, the theory contains multiple unconstrained parameters (e.g., updraft area fraction, an ‘entrainment’ parameter representing dissipative effects on cloudy updrafts) that would vary greatly on time scales larger than those of a single event. To the best of our knowledge, Cannon et al. (2014) is the only analytical work focused on orographic deep convection, having developed an area-averaged model with detailed microphysics. The precipitation rate is computed level-wise by bringing parcels to their level of neutral buoyancy, then accounting for detrainment and evaporation due to compensating descent before applying a CAPE-dependent weighting. The

model leads to a high number of equations to be solved, hindering physical insights, and its “bulk” nature obscures key questions such as how far upstream precipitation is enhanced and how long the rain shadow is.

A fruitful line of development in the theory of tropical dynamics has been the quasiequilibrium (QE) view of convection, dating back to Arakawa and Schubert (1974) and outlined by Emanuel et al. (1994). This view has its roots in the observation that CAPE often varies slowly compared to its generation mechanisms (i.e. tropospheric radiative cooling, surface enthalpy fluxes, and large-scale ascent), with CAPE anomalies consumed as convective activity responds rapidly to any change in the generation mechanisms. An ensemble of convective motions is thus in near statistical equilibrium with the large-scale forcings, with convective motions setting the vertical temperature profile, tying it directly to the subcloud-layer moist static energy. QE theories seem most relevant for relatively slow forcings such as the seasonal cycle, which evolves on a time scale orders of magnitude longer than that of the convective response. This motivates our use of QE theory here to describe time-mean patterns of orographic precipitation, which in some regions (e.g. South Asia) constitutes a substantial fraction of the regional total precipitation (Xie et al. 2006), that has in turn been understood using QE frameworks (e.g. Nie et al. 2010). Specifically, we use QE theory to describe the statistical average effect of mountains on time-mean convective precipitation, rather than formulating a theory of event-wise convective triggering by orographic ascent. While early QE theories employed CAPE-based convective closures, we leverage recent developments that incorporate observed relationships between precipitation and lower-tropospheric temperature and humidity (Derbyshire et al. 2004; Raymond et al. 2015; Ahmed et al. 2020). We discuss further details and possible caveats, such as whether Eulerian or Lagrangian time scales are relevant for evaluating the validity of QE, later in the context of results from our idealized model.

Here we pose two key questions: what sets the mean precipitation rate of mechanically forced orographic convection? How far upstream and downstream does orography influence tropical precipitation? Unlike some classic QE closures that only consider near-surface temperature and moisture anomalies, we use a convective closure that is sensitive to lower free tropospheric anomalies, and accounts for the influence of stationary orographic gravity waves on those anomalies. This links classic stationary wave theory with modern QE closures for convection, and provides nonlinear expressions for precipitation as well as a linearized theory that can be forced by the Fourier transformed terrain. Convection-permitting simulations in a long channel are used to test theoretical rain rates. We use the results of these simulations to evaluate the convective time scales used in the theory and the possible influence of spatial modulations of surface evaporation and radiative cooling downwind of the ridge.

## 2. Theory

This section presents an analytical theory for the precipitation over a tropical mountain in a background wind, based on a QE convective closure. Its aim is to account for the main features of time-mean precipitation around the ridge (peak value, spatial extent of upstream enhancement, rain shadow length), as a function of large-scale flow characteristics and ridge shape. The theory is based loosely on the Quasiequilibrium Tropical Circulation Model (QTCM) of Neelin and Zeng (2000), but employs the moisture-temperature ( $q - T$ ) convective parameterization proposed by Ahmed et al. (2020). This closure was derived from the empirical relationship between precipitation and lower-free-tropospheric buoyancy and parameterizes precipitation as a response to both temperature and moisture perturbations, with different sensitivities. The reason we chose to use this closure instead of a more classic CAPE-based parameterization will be expanded upon in section 3b.

Our main hypothesis, assessed in later sections, is that mountains alter convection by modulating lower-tropospheric temperature and moisture. In the presence of a background wind, an orographic gravity wave is excited that carries thermodynamic perturbations. Forced ascent upwind of the ridge cools and moistens the lower free troposphere, enhancing convection. The opposite occurs downstream where subsidence prevails. In addition to these orographically induced thermodynamic variations, we will show that the solution depends on the convective adjustment time scales and on an advective length scale, with the latter being the product of the background wind speed with a time scale for relaxation to radiative-convective equilibrium (RCE). The mountain wave may also modify the tropospheric static stability and wind shear, but we focus on lower-tropospheric temperature and moisture anomalies because these have been found to exert a strong control on deep convection (Derbyshire et al. 2004; Raymond et al. 2015; Ahmed et al. 2020).

### *a. Modal decomposition*

Throughout this paper, we consider a horizontally infinite low-latitude domain with surface elevation  $h(x)$  and a uniform and constant background horizontal wind  $\mathbf{u}_0$ . As explained in Appendix A, linearizing the dynamics allows the flow to be described as the sum of a basic state and two perturbation modes: a dry mode, due solely to the orographic gravity wave, and a moist mode, that represents the moist convective part of the flow. The dry mode only influences the moist mode as a forcing for convective heating, while the moist mode does not influence the dry mode. The latter assumption is not entirely justified, as we will show in section 3c that the orographic gravity wave feels a lower effective stability due to the presence of moist convection, in a convection-permitting numerical model. Steady-state thermodynamic and moisture equations

for the moist mode are

$$\mathbf{u}_0 \cdot \nabla T_m + \omega_m \frac{\partial s_0}{\partial p} = Q_c - R, \quad (1a)$$

$$\mathbf{u}_0 \cdot \nabla q_m + \omega_m \frac{\partial q_0}{\partial p} = Q_q + E, \quad (1b)$$

where  $s_0(p)$  and  $q_0(p)$  are, respectively, the reference dry static energy and moisture vertical profiles, with the zero subscript denoting a property of the basic state, and  $\omega_m$ ,  $T_m$ , and  $q_m$  are the pressure velocity, temperature, and moisture perturbations of the moist mode.  $Q_c$  and  $Q_q$  denote convective heating and moistening, while  $R$  and  $E$  are radiative cooling and evaporation rates. Here, and subsequently, temperature and moisture are in energy units (i.e. they have, respectively, absorbed the heat capacity of air at constant pressure  $c_p$ , and the latent heat of vaporization of water  $L_v$ ). This linearized formulation neglects horizontal variations in static stability and moisture stratification caused by orography, which in the simulations presented in Section 3 are of order 20% downstream of the ridge (with local increases up to 30% above the ridge).

We now perform a unimodal vertical truncation of the moist mode. We only include a deep convective mode, with any shallow temperature anomaly induced by the orographic gravity wave represented by the dry mode. This treatment likely renders our theory most appropriate for deep tropical regions, where deep convection is observed to generate most rainfall (Tan et al. 2013; Houze et al. 2015), in contrast with the midlatitudes or trade wind regions (e.g. Kirshbaum and Smith 2009). Following Sobel et al. (2001), we also employ the weak temperature gradient (WTG) approximation for the moist mode, which allows us to solve for that mode without the momentum equations (remember that horizontal temperature gradients induced by the orographic gravity wave are carried by the dry mode). Using notation from Neelin and Zeng (2000), we write

$\omega_m(x, y, p) = \omega_1(x, y)\Omega_1(p)$  and vertically average (1a)-(1b), yielding

$$-\omega_1 M_s = \langle Q_c \rangle - \langle R \rangle, \quad (2a)$$

$$\mathbf{u}_0 \cdot \nabla \langle q_m \rangle + \omega_1 M_q = \langle Q_q \rangle + \langle E \rangle, \quad (2b)$$

with  $\langle \cdot \rangle = \int_{p_t}^{p_s} \{\cdot\} dp / p_T$ . Here  $p_T = p_s - p_t$  is the tropospheric depth, and  $p_s$  and  $p_t$  are, respectively, surface and tropopause pressures (the tropospheric mass per unit area is  $p_T/g = 8000 \text{ kg m}^{-2}$  henceforth.). The gross dry stability and gross moisture stratification are respectively defined by  $M_s = \langle \Omega_1 \partial s_0 / \partial p \rangle$  and  $M_q = \langle \Omega_1 \partial q_0 / \partial p \rangle$ . The quantity  $M = M_s - M_q$  is known as the gross moist stability (GMS, see e.g. Neelin and Held 1987; Raymond et al. 2009).

We now introduce the energy constraint  $\langle Q_c \rangle = -\langle Q_q \rangle$  and employ the  $q-T$  convective closure,

$$\langle Q_c \rangle = \left( \frac{q'_L}{\tau_q} - \frac{T'_L}{\tau_T} \right)_+, \quad (3)$$

where  $(\cdot)_+ = \max(\cdot, 0)$ .  $\tau_q$  and  $\tau_T$  are the moisture and temperature adjustment time scales, diagnosed respectively as approximately 11 hours and 3 hours by Ahmed et al. (2020).  $q'_L$  and  $T'_L$  are total deviations (the sum of perturbations in both the moist and dry modes) from the reference profiles of moisture and temperature, with  $(\cdot)_L = \int_{p_{Lb}}^{p_{Lt}} \{\cdot\} dp / (p_{Lt} - p_{Lb})$  denoting a lower-free-tropospheric average, where  $p_{Lb} = 900 \text{ hPa}$  and  $p_{Lt} = 700 \text{ hPa}$ . Decomposing these anomalies into contributions from the moist and dry modes (subscripts  $m$  and  $d$ , respectively, see also Appendix A) gives

$$q'_L = q_{mL} + q_{dL} \text{ and } T'_L = T_{mL} + T_{dL} = T_{dL}, \quad (4)$$

where the last equality comes from WTG (if  $\nabla T_m = 0$ , one can add any horizontally uniform nonzero  $T_m(p)$  to the reference profile  $T_0(p)$ , hence resulting in  $T_m = 0$ ). The heating term (3) will have two contributions: one from the dry perturbations  $q_{dL}$  and  $T_{dL}$  (hereafter referred to as “the dry forcing for convection”), and a moist convective response carried by  $q_{mL}$ . Because we

assumed a horizontally and temporally invariant vertical profile for  $q_m$ , the quantities  $q_{mL}$  and  $\langle q_m \rangle$  are proportional. Using the notation of Ahmed et al. (2020),  $q_{mL}/\tau_q = \langle q_m \rangle/\tilde{\tau}_q$ , where  $\tilde{\tau}_q \simeq 0.6\tau_q$ .

### b. A general precipitation equation

We can now obtain an equation for precipitation, which is related to the convective heating by  $P = p_T \langle Q_c \rangle / g$  in units of energy per unit area per unit time (dividing by  $\rho_w L_v$ , where  $\rho_w$  is the density of liquid water, yields a physical precipitation rate, in  $\text{m s}^{-1}$ ). Using (3), (4) and the definition of  $\tilde{\tau}_q$ , we obtain

$$P = \frac{p_T}{g} \left( \frac{\langle q_m \rangle}{\tilde{\tau}_q} + \frac{q_{dL}}{\tau_q} - \frac{T_{dL}}{\tau_T} \right)_+. \quad (5)$$

We then eliminate  $\omega_1$  in (2a)-(2b) and use (5) to obtain an equation for  $P$  that involves only the various imposed thermodynamic parameters, incident wind, and perturbations in the dry mode:

$$\begin{aligned} \mathbf{u}_0 \cdot \nabla P &= \left[ -\frac{M}{M_s \tilde{\tau}_q} (P - P_0) + \frac{p_T}{g} \mathbf{u}_0 \cdot \nabla \left( \frac{q_{dL}}{\tau_q} - \frac{T_{dL}}{\tau_T} \right) \right] \mathcal{H}(P), \\ \text{where } P_0 &= \frac{p_T}{g} \frac{M_s \langle E \rangle - M_q \langle R \rangle}{M} \end{aligned} \quad (6)$$

and  $\mathcal{H}$  denotes the Heaviside function. We henceforth drop the  $y$  dependence, simplifying (6) to

$$\begin{aligned} \frac{dP}{dx} &= \left[ -\frac{P - P_0}{L_q} + \frac{p_T}{g} \frac{d}{dx} \left( \frac{q_{dL}}{\tau_q} - \frac{T_{dL}}{\tau_T} \right) \right] \mathcal{H}(P), \\ \text{where } L_q &= u_0 \tilde{\tau}_q \frac{M_s}{M}. \end{aligned} \quad (7)$$

Note that in a state of RCE,  $\langle E \rangle = \langle R \rangle$ , hence the basic state precipitation  $P_0 = p_T \langle E \rangle / g$ , which is the column-integrated evaporation rate. (7) is essentially a forced equation with  $P$  relaxed towards  $P_0$  on the length scale  $L_q$ . Hence, if the dry forcing  $\langle q_d \rangle / \tau_q - \langle T_d \rangle / \tau_T$  is felt on a distance significantly shorter than  $L_q$ , the latter will dominate in setting the length of the downstream rain shadow.

$L_q$  can be understood as a Lagrangian convective length scale, whereby a column traveling at velocity  $u_0$  undergoes moisture adjustment on a time scale  $\tilde{\tau}_q$ . It is also inversely proportional to the

relative GMS  $M/M_s$ , which measures the efficiency with which a column exports energy through divergent flow, and thus returns to an equilibrium state.  $L_q$  is vanishingly small, and the dry forcing is felt on equally small distances, in the limit of zero wind (no advection), instantaneous convective adjustment, or infinite GMS (allowing for instantaneous return to equilibrium). We estimate a ratio  $M/M_s = 5$  (see section 4c) so that for  $u_0 = 10 \text{ m s}^{-1}$ ,  $L_q \simeq 1000 \text{ km}$ . As suggested in the preceding paragraph,  $L_q$  places a lower bound on the rain shadow length; such an extensive rain shadow may seem unrealistic, but in real cases large-scale processes and flow detouring around topography can shorten the rain shadow. A time-varying cross-slope wind, including episodes of reversed flow, would further shorten the time-mean rain shadow. Note however that precipitation is reduced over about 1000 km downwind of the Western Ghats (Figure 1c). This is consistent with the very broad rain shadow downwind of Sri Lanka during the Indian summer monsoon (e.g. Biasutti et al. 2012).

### *c. A linear theory*

Equation (7) can be solved for the precipitation field as a function of moisture and temperature perturbations induced by “dry” mountain flow. These perturbations can in turn be obtained with several degrees of complexity, from a full mountain wave simulation to a linear solution with uniform background stratification. Here, in the spirit of the linear model of SB04, we employ linear mountain wave theory to obtain a closed expression relating mountain shape to precipitation in the Fourier domain.

The linearized thermodynamic and moisture equations of the dry mode (see Appendix A) read

$$u_0 \frac{dT_d}{dx} + w_d \frac{ds_0}{dz} = 0, \quad u_0 \frac{dq_d}{dx} + w_d \frac{dq_0}{dz} = 0, \quad (8)$$

where we used height coordinates and dropped the  $y$  dependence. Hence, the dry forcing for convection in (7) becomes

$$\frac{d}{dx} \left( \frac{q_{dL}}{\tau_q} - \frac{T_{dL}}{\tau_T} \right) = \frac{w_{dL}}{u_0} \left( \frac{1}{\tau_T} \frac{ds_0}{dz} - \frac{1}{\tau_q} \frac{dq_0}{dz} \right), \quad (9)$$

where we have assumed that  $ds_0/dz$  and  $dq_0/dz$  do not depend on  $z$ . This assumption may seem crude for the moisture profile, which usually decays rapidly in height, but it is accurate given an appropriate choice for  $w_{dL}$ ; it furthermore retains the first-order physical picture that lower-tropospheric ascent leads to moistening. We define the constant  $\chi$  as the sum of two terms both contributing to enhanced convection,

$$\chi = \frac{p_T}{g} \left( \frac{1}{\tau_T} \frac{ds_0}{dz} - \frac{1}{\tau_q} \frac{dq_0}{dz} \right). \quad (10)$$

These two terms represent, respectively, lower tropospheric cooling (due to adiabatic ascent), and moistening (also due to ascent along a vertically decreasing moisture profile,  $dq_0/dz < 0$ ). To obtain a linear equation, the nonlinear Heaviside function in (7) has to be dropped; this amounts to allowing negative  $Q_c$ , which only influences the solution in the downstream region, where drying and warming by the dry mode predominate. We now substitute (9) and (10) into the linearized (7) and take the Fourier transform, yielding

$$ik\hat{P}'(k) + \frac{\hat{P}'(k)}{L_q} = \frac{\hat{w}_{dL}(k)}{u_0}\chi, \quad (11)$$

where  $P' = P - P_0$ ,  $k$  is the horizontal wavenumber and the Fourier transform is denoted with a hat. Linear, Boussinesq mountain wave theory expresses  $\hat{w}_d$  as (e.g., Smith 1979)

$$\hat{w}_d(k, z) = iku_0\hat{h}(k)e^{im(k)z}$$

and  $m(k) = \begin{cases} \sqrt{l^2 - k^2} & \text{if } k^2 < l^2 \\ i\sqrt{k^2 - l^2} & \text{if } k^2 > l^2 \end{cases}, \quad (12)$

where  $l = N/u_0$  and  $N$  is the Brunt-Väisälä frequency, assumed positive and constant with height.  $N$  is related to the basic state lapse rate by  $N^2 \simeq (g/T_r)ds_0/dz$ , with  $T_r$  a reference temperature taken as  $c_p \times 300$  K. We have also assumed that the density of air is uniform, given that perturbations are averaged over the lower troposphere only. Combining (11) and (12) gives the final relationship:

$$\hat{P}'(k) = \frac{ik\chi}{ik + 1/L_q} \hat{h}(k) \left( e^{im(k)z} \right)_L. \quad (13)$$

After solving for  $P'$ , negative values of precipitation are avoided by applying the  $(\cdot)_+$  operator to  $P' + P_0$ . The above linear expression for convective orographic precipitation is meant to represent time-mean rain rates, as opposed to single-event or extreme precipitation. It depends on two parameters ( $\tau_q$  and  $\tau_T$ ) and a number of physical quantities:  $u_0$ ,  $N$ , the moisture lapse rate  $dq_0/dz$ , the mountain profile  $h(x)$ , and, through  $L_q$ , the relative GMS  $M/M_s$ . We now explore sample solutions with idealized mountain profiles to illustrate predictions of this theory.

#### *d. Example profiles*

We now illustrate the behavior of (13), obtaining quantitative estimates for the influence of the convective response times, the location and magnitude of the maximum precipitation, and the upstream distance over which precipitation is enhanced. For the mountain shape, we choose the classic Witch-of-Agnesi profile  $h(x) = h_0 l_0^2 / (x^2 + l_0^2)$ , where  $l_0$  is the mountain half-width and  $h_0$  is the maximum height. The basic state wind  $u_0$  is set to  $10 \text{ m s}^{-1}$ , and the relative GMS, which influences the Lagrangian convective length scale  $L_q$ , is set to  $M/M_s = 0.2$ , a representative value for tropical regions.. We set  $N = 0.01 \text{ s}^{-1}$ , or equivalently  $ds_0/dz \simeq 3 \text{ J kg}^{-1}\text{m}^{-1}$  or  $3 \text{ K km}^{-1}$ . The lower tropospheric average in (13) is taken, for convenience, between two constant height (rather than constant pressure) surfaces at  $z = 1000 \text{ m}$  and  $3000 \text{ m}$ . The moisture lapse rate is computed as an average over the same layer of the profile  $q_0(z) = r q_{\text{sat}}(T_s) e^{-z/H_m}$  where  $r = 0.8$ ,  $T_s = 300 \text{ K}$

and  $H_m = 2500$  m, which yields  $dq_0/dz \simeq 8.1 \text{ J kg}^{-1}\text{m}^{-1}$ . Finally, the equilibrium precipitation  $P_0 = 4 \text{ mm day}^{-1}$ .

Using a fast Fourier transform (FFT), we compute solutions with two different mountain heights and varying  $\tau_T$  and  $\tau_q$  (thick solid curves in Fig. 2). The reference case uses  $l_0 = 50 \text{ km}$ ,  $h_0 = 1000 \text{ m}$ , and  $\tau_T = 3 \text{ hours}$  and  $\tau_q = 11 \text{ hours}$  (with the latter two computed by Ahmed et al. 2020, yielding  $L_q = 1188 \text{ km}$ ). Precipitation is significantly enhanced starting 1500 km upstream and peaks near the steepest slope of the ridge's windward side, with a 7-fold enhancement compared to the undisturbed  $P_0$ . Downwind, the rain shadow is about 1000 km long and precipitation overshoots  $P_0$  before slowly relaxing back towards it. This behavior can be understood as follows: precipitation is suppressed immediately downstream of the mountain because of the warm and dry lower free-troposphere created by the gravity wave, then humidity builds in response to the reduced convective drying (in the presence of the ongoing surface evaporation) past its RCE level to compensate for the warm anomaly. The latter dissipates as the flow progresses further downwind, allowing for a convective overshoot.

A second case shows that increasing the convective time scales by 50% mainly produces a proportional decrease in the upstream precipitation perturbation. This occurs because, in the linear solution (13),  $P'$  is proportional to  $\chi$ , which is in turn inversely proportional to the time scales; convection responds more weakly to the dry gravity wave as the time scales are increased, as specified in the simple convective closure (3). Additionally, the increase in  $\tau_q$  results in an increase in  $L_q$ , which primarily lengthens the rain shadow. The third example in Fig. 2 (with  $h_0 = 500 \text{ m}$ ) confirms that, in this linear framework, halving  $h_0$ , while keeping other parameters constant, exactly halves  $P'$ .

Linear flow over a Witch-of-Agnesi ridge admits approximate analytical solutions, allowing us to diagnose the various scales involved in the upstream precipitation response. We perform an

inverse Fourier transform of (11) and then integrate, yielding

$$\begin{aligned} P' &= \chi \int_{-\infty}^x \frac{w_d L(x')}{u_0} e^{-\frac{x-x'}{L_q}} dx' \\ &= \chi \zeta_L(x) - \chi \int_{-\infty}^x \frac{\zeta_L(x')}{L_q} e^{-\frac{x-x'}{L_q}} dx' \end{aligned} \quad (14)$$

after integrating by parts and noting that  $w_d(x', z) = u_0 \partial \zeta(x', z) / \partial x'$ , where  $\zeta(x', z)$  is the vertical displacement at  $x'$  of a streamline originating upstream at  $z$ . For mesoscale ridges satisfying  $l_0 N/U \gg 1$ ,  $\zeta_L$  can be approximated as (Queney 1948)

$$\zeta_L(x) = h_0 \frac{cl_0^2 - sl_0 x}{x^2 + l_0^2}, \quad (15)$$

where  $c = (\cos(Nz/U))_L$  and  $s = (\sin(Nz/U))_L$ . The first term on the right-hand side of (14) is proportional to the lower-tropospheric averaged vertical displacement; it scales like the cold and moist anomaly created by the mountain wave, to which precipitation would be proportional in the absence of any moist mode anomalies. This term represents a distinct influence of the mountain wave on precipitation compared to that portrayed in the traditional literature on orographic precipitation: this influence is a function of vertical displacement, not vertical velocity. The second term acts as a damping: the moist mode responds to enhanced precipitation with a negative humidity anomaly ( $\langle q_m \rangle < 0$ ) that develops on a length scale  $L_q$ . In the limit  $l_0/L_q \rightarrow 0$ , this term becomes negligible as the moist mode responds too slowly (in a Lagrangian sense) to the perturbation induced by the gravity wave. However, even for the small value of  $l_0/L_q \simeq 0.05$  used here, this second term provides a sizeable precipitation reduction (compare the dashed line, which represents the solution without this second term, with the solid line of the same color in Figure 2).

Because the second term in (14) varies on large scales of order  $L_q$ , the location of the precipitation maximum,  $x_{\max}$ , will be set to first order by the location of maximum vertical displacement  $\zeta_L$  for

cases where  $l_0/L_q \ll 1$ . One obtains

$$x_{\max} = -l_0 \left( \sqrt{1 + \frac{c^2}{s^2}} - \frac{c}{s} \right). \quad (16)$$

With the above parameters,  $x_{\max}$  lies 76 km upstream of the mountain peak, i.e. slightly upstream of the steepest slope  $x = -l_0/\sqrt{3}$  (note that with this value of  $N/U$ ,  $s > 0$  and  $c < 0$ ). The amplitude of the precipitation maximum,  $P_{\max}$ , will be more affected by the moist-mode damping; neglecting that damping provides an upper bound,

$$P_{\max} \leq P_0 + \chi h_0 s / [2(\sqrt{1+c^2/s^2} - c/s)]. \quad (17)$$

This expression overestimates the true precipitation maximum by about 30% for the above cases (dashed line in Figure 2).

We can also obtain from (14) an order of magnitude for the upstream extent of the precipitation enhancement, defined as the location  $x_u$  where  $P'$  exceeds a threshold  $\delta P$ . Far upstream of the ridge (i.e.  $x \ll -l_0$ ), approximating  $\zeta_L \simeq -h_0 l_0 s / x$  gives

$$\begin{aligned} P'(x) &\simeq -\frac{\chi s h_0 l_0}{L_q} \left[ \frac{L_q}{x} - e^{-x/L_q} \text{Ei}(x/L_q) \right] \\ &\simeq -\frac{\chi s h_0 l_0}{L_q} \left[ \frac{L_q}{x} + \ln \left( 1 - \frac{L_q}{x} \right) \right] \\ &\leq \frac{\chi s h_0 l_0}{2L_q} \left( \frac{L_q}{x} \right)^2. \end{aligned} \quad (18)$$

Where  $\text{Ei}$  is the exponential integral function, and the approximation used in the second equality is given in Abramowitz and Stegun (1964). The inequality on the last line is valid for  $x \leq 0$ . Hence, an upper bound on the upstream extent is

$$|x_u| \leq \sqrt{L_q l_0 \frac{\chi s h_0}{2\delta P}}. \quad (19)$$

The right-hand side of (19) is the geometric mean of two terms, one scaling the upstream extent of the orographic enhancement in the absence of damping and the other one being  $L_q$ . The larger

$L_q$ , the less effective the damping, hence the farther upstream a given value of  $\delta P$  is attained; in the absence of any moist damping (i.e.  $L_q/l_0 \rightarrow \infty$ ),  $x_u = l_0\chi sh_0/\delta P$ . With the above values for  $\chi$ ,  $s$ , and  $l_0$ , and for  $h_0 = 1000$  m and  $\delta P = 1$  mm day $^{-1}$ , (19) gives  $|x_u| \leq 1746$  km. The very good agreement with the true value, of about 1700 km, is due to cancellation between the two approximations made in (18); (19) overestimates the true  $|x_u|$  by about 20% in the two other cases shown in Figure 2.

#### e. Summary

The theory presented in this section uses a quasiequilibrium closure to solve for the convective precipitation forced by a dry orographic gravity wave, through its modulation of lower tropospheric temperature and moisture. The most general equation is (6); it retains the nonlinearity of the convective closure and applies to flows with two horizontal dimensions. Dropping a horizontal dimension leads to (7) and introduces  $L_q$ , the Lagrangian convective length scale on which precipitation converges to its equilibrium value  $P_0$ ; this is also the rain shadow length scale in cases where the dry forcing is felt on small distances. This nonlinear theory lacks a closure for the dry perturbations induced by the orographic gravity wave.

Treating the orographic gravity wave linearly, and neglecting the nonlinearity of the convective closure, yields equation (13); this is a closed theory relating mountain shape to the spatial profile of convective precipitation, in the spirit of SB04. The theory depends on a number of physical quantities and the time scales of the convective closure,  $\tau_T$  and  $\tau_q$ . Whilst (13) can be solved numerically with a FFT, approximate analytical expressions are obtained in the case of a Witch-of-Agnesi terrain, yielding expressions for the location of the precipitation maximum and the upstream extent of the precipitation enhancement. For some typical tropical parameter values and a 1000 m high, 200 km wide ridge, precipitation is enhanced about 2000 km upstream of the mountain, the

peak precipitation occurs slightly upstream of the steepest slope on the upwind side, and the rain shadow is around 1000 km wide. The peak precipitation magnitude depends on parameters that are relevant both to the dry dynamics (wind speed, static stability, mountain height) and the moist dynamics (convective adjustment time scales, relative GMS).

### 3. Numerical simulations

This section presents the framework we use to test the theory: a set of convection-permitting simulations in which a constant horizontal background flow in a long channel encounters a ridge. In addition to comparing simulated precipitation from this model with our theory, we evaluate the validity of the QE and WTG approximations.

#### *a. Simulation setup*

We use a three-dimensional idealized version of the Weather Research and Forecasting model (WRF-ARW, version 4.1.5, Skamarock et al. 2019), which is fully compressible and nonhydrostatic. The domain is periodic in  $x$  and  $y$  directions, 9810 km long and 198 km wide with a 3 km horizontal grid spacing. A single  $y$ -invariant ridge is present. It uses 60 hybrid terrain-following/pressure vertical levels stretching from the surface to 10 hPa, corresponding to about 28 km. The domain length is chosen so the flow fully recovers to an undisturbed state after encountering the mountain ridge, before circling back in the periodic domain. Comparisons of its vertical structure 3000 km upstream (or, equivalently 6810 km downstream) of the ridge with a flat, ocean-covered simulation (not shown) shows no appreciable difference, confirming the domain length is sufficient. The  $y$  dimension is large enough for several convective clouds of sizes  $O(1 - 10)$  km to develop in that cross-stream direction. The 3 km grid spacing is a compromise between the need for realistic simulation of convection and the computational cost of long time integrations. This resolution has

been widely used in large-domain convection-permitting simulations (Satoh et al. 2019), including geometries similar to ours (Wing and Cronin 2016; Wang and Sobel 2017). Kirshbaum (2020) found that in idealized cases of mechanically forced orographic convection (though at smaller spatial scales and time scales) with interactive surface fluxes (i.e., their MECH-FLX simulations), a resolution of 2 km gave similar along-stream precipitation profiles to runs at much smaller grid spacing  $O(100$  m). Zhang and Smith (2018) found that resolutions of 2 km vs 6 km made little difference in simulating orographic convection over the Western Ghats.

Surface elevation is

$$h(x) = \begin{cases} \frac{h_0}{2} \left(1 + \cos\left(\pi \frac{x}{l_0}\right)\right) & \text{if } |x| < l_0, \\ 0 & \text{otherwise,} \end{cases} \quad (20)$$

where  $l_0 = 100$  km (which yields a similar topography to a Witch-of-Agnesi ridge of half-width 50 km). Hereafter,  $x$  runs from  $-4405$  km to  $4405$  km with the mountain at  $x = 0$ . Such one-dimensional terrain forces all parcels to ascend the ridge, rather than detouring around it, but provides a first step towards better understanding the interaction of deep convection with orography. The mountain's surface (i.e., where  $|x| < l_0$ ) is covered with land. To obtain a closed surface energy budget and avoid having to choose a surface temperature lapse rate, the land surface is parameterized with the NoahMP scheme (Niu et al. 2011; Yang et al. 2011), using four soil levels and a no-flux bottom boundary condition at the lowest level. The rest of the domain is ocean-covered with fixed sea-surface temperature of 300 K.

The Coriolis force is applied to deviations from a uniform geostrophic wind  $u_0 = -10$  m s $^{-1}$  (i.e., an easterly wind), with fixed Coriolis parameter  $f = 4.97 \cdot 10^{-5}$  s $^{-1}$  (corresponding to 20°N). This is equivalent to imposing a background meridional pressure gradient, which maintains a constant background geostrophic flow. Microphysics are computed using the single-moment Thompson et al. (2008) scheme, surface layer mixing employs the MM5 similarity theory (Jiménez et al. 2012),

and boundary layer fluxes are parameterized with the Mellor-Yamada-Janjić scheme (Mellor and Yamada 1982; Janjić 2002). The model is run without a turbulence scheme (although the surface layer and PBL schemes do parameterize turbulent mixing), but comparing the first 20 days of simulation with a run having nonzero turbulent diffusion does not show any appreciable difference. Radiation is computed interactively every minute with the RRTMG scheme (Iacono et al. 2008). All simulations have a diurnal cycle of insolation but no seasonal cycle (the solar declination angle is fixed to  $0^\circ$ , a state of perpetual equinox).

We perform two “control” simulations, one with mountain height  $h_0 = 1000$  m and the other with  $h_0 = 500$  m. The first case is close to several mountain ranges of South Asia (Western Ghats, Annam Range, Arakan Yoma) and yields a nondimensional mountain height  $Nh_0/u_0 \simeq 1.2$ . This suggests moderate flow blocking by the ridge and possible flow splitting if the mountain were not infinite in  $y$  (Smith 1989), indicating a limitation of our setup. This limitation has implications for lee-side flow: Epifanio and Durran (2001) showed that downstream temperature perturbations are higher with a  $y$ -invariant ridge than when the flow is allowed to split, even with mountains of high aspect ratio. Upstream flow could also be decelerated more rapidly for the infinite ridge. However, our use of rotation prevents the development of an upstream-propagating bore (Pierrehumbert and Wyman 1985), and instead sets up a barrier jet (see also section 3b). Convection may also reduce the nonlinear effects that occur for a high nondimensional mountain height by lowering the effective stability felt by the flow, as explained in section 3c.

The  $h_0 = 500$  m case is perhaps a better test for the linear theory and more realistic because it exhibits reduced blocking ( $Nh_0/u_0 = 0.6$ ) and thus is farther from the limit of a high, infinitely long ridge; in this regime, high aspect ratio and  $y$ -infinite ridges have similar lee-side flows (Epifanio and Durran 2001). Both simulations are integrated for 200 days with statistics collected after spinup of 50 days.

An additional simulation with  $h_0 = 1000$  m is run with latent heating turned off (the “ $L_v = 0$  simulation”) to assess the effect of the mountain on the flow in the absence of moist convection. It is initialized with mean temperature and moisture soundings from the control and run for 100 days, with radiation and surface fluxes turned off. Water can still condense and fall, and virtual temperature effects are retained. The temperature profile warms in the boundary layer by about 3 K in this run, but sees little change aloft; the vertical profile of  $N$ , which controls the mountain-induced dry gravity wave (Durran 2003), is little altered.

### *b. Precipitation and CAPE*

Meridionally averaged and time averaged (from days 50 to 200) precipitation and CAPE from the  $h_0 = 500$  m and 1000 m runs are shown in Figure 3. Here, and subsequently, the  $x$ -axis is oriented so the background wind flows left to right; i.e. East is on the left, and West on the right.  $P_n$  denotes precipitation in the  $n$  m run. Both CAPE and precipitation are nearly constant more than 4000 km downstream of the mountain peak and more than 1500 km upstream. This, together with the absence of mean upward motion in that region (not shown), indicates a state of RCE far from the mountain. This supports our claim that the periodic domain is long enough for the flow to recover from the disturbance imparted by the ridge.

We now discuss some key features of the precipitation profiles. Upstream-averaged precipitation (i.e., from 2000 to 5000 km upwind of the peak) is about  $P_0 = 4.5 \text{ mm day}^{-1}$  for both runs. The orographic enhancement exceeds  $1 \text{ mm day}^{-1}$  starting 670 km and 720 km upstream for  $P_{500}$  and  $P_{1000}$ , respectively. The length scale of this upstream enhancement is an order of magnitude larger than typically observed in midlatitudes (e.g., SB04) or in shallow-convective tropical flows (e.g., Kirshbaum and Smith (2009)). It is consistent with observational profiles from Figure 1. Section 2 suggests this is due to the sensitivity of deep convection to thermodynamic perturbations from the

mountain wave that are felt far upstream; section 4 will examine this hypothesis in greater detail. Both runs have pronounced rainfall peaks (about  $12 \text{ mm day}^{-1}$  and  $20 \text{ mm day}^{-1}$ , respectively) on the upwind mountain slope, about 55 km upstream of the peak (slightly upwind of the maximum slope). In the rain shadow region, the negative anomalies are smaller in the  $h_0 = 500 \text{ m}$  run than in the  $h_0 = 1000 \text{ m}$  run, as expected from the linear theory. Both runs return to the background value  $P_0$  around the same location, 2000 km downstream. Unlike the linear runs with a Witch-of-Agnesi profile, there is no clear overshoot past  $P_0$  downstream. This is mostly due to the different mountain shapes employed, as we will see that this overshoot vanishes when applying (13) to the cosine terrain shape (20) in part 4c. Both runs display a small rainfall peak immediately downstream of the ridge. This feature is likely related to nonlinear dynamics, perhaps involving a hydraulic jump causing strong upward motion at this location (see Kirshbaum et al. 2018). We do not devote further attention to it, given its small amplitude and limited spatial extent.

Under the assumptions of linearity made in section 2c, changing the mountain height should scale the orographically modified precipitation proportionately, so  $P_{1000} - P_0 = 2(P_{500} - P_0)$ . Figure 3 shows this test of linearity, in which  $P_{1000}$  is approximated by  $(2P_{500} - P_0)_+$ , alongside the simulated  $P_{1000}$ . There is remarkable agreement, with the prediction lying within the uncertainty bounds of  $P_{1000}$  at nearly all locations. This provides confidence in the relevance of linear theory to mechanically forced orographic convection (we compare with our theory in detail in Section 4).

The presence of a barrier jet in our simulations (not shown) raises the question of its influence on precipitation (e.g. Neiman et al. 2013). Consistent with theory (Pierrehumbert and Wyman 1985), it extends to a Rossby deformation radius, about 2000 km, upstream of the mountain. No significant departure from the background precipitation is detectable this far upstream. Good agreement on the upstream extent of precipitation between the linear theory and the simulations (see section 4c) is another indication that barrier jet dynamics have little effect on rainfall in these runs. Barrier

jets might, however, have greater importance for more nonlinear flows, with stronger jets leading to enhanced or shifted rainfall patterns (as shown for the Sierra Nevada mountains by Neiman et al. 2013).

Examination of the diurnal cycle of precipitation in the  $h_0 = 1000$  m run can serve as a probe of the importance of thermal forcing for convection. Between the mountaintop and 200 km upstream, the diurnal cycle of precipitation has an amplitude of 20% of the time-mean value. This is smaller than in the RCE part of the domain, where the relative amplitude is 25%, and suggests a small role for island surface fluxes in producing rainfall. For comparison, Wang and Sobel (2017) simulated thermally forced convection over isolated islands and reported relative amplitudes of the diurnal cycle of around 80%.

We also show CAPE in Figure 3 to illustrate the difficulty of using CAPE-based closures in theory for orographic precipitation. Despite the cooling effect of the gravity wave on the lower free troposphere upstream of the mountain (analyzed in more detail in Section 4c), CAPE gradually decreases starting 500 km upstream and drops to almost zero above the mountain. This can be understood as a progressive consumption of CAPE by enhanced convection, triggered by reduced convective inhibition (CIN; Ahmed et al. (2020) highlight the similarity of the  $q - T$  closure to CIN-based convective parameterizations). Downstream of the ridge, reduced convection allows CAPE to build and even overshoot its upstream value, much like the linear theory for precipitation (Figure 2). CAPE-based closures typically diagnose precipitation as the ratio of CAPE to a convective time scale; the latter would have to vary spatially here to accommodate the absence of proportionality between CAPE and P. The time scale would have to decrease upstream of and above the mountain (e.g., due to orography “triggering” convection by mechanical forcing) and increase downstream. The challenge of such an approach is that the rainfall profile is highly sensitive to spatial variations of the time scale, rendering derivation of a physically based closure difficult.

### c. Vertical motion

Figure 4 shows time and meridionally averaged vertical velocity in the  $h_0 = 1000$  m control run and the  $L_v = 0$  run. Interaction of the basic state flow with the mountain produces a gravity wave in the  $L_v = 0$  run that influences the flow between about 500 km upstream and 2000 km downstream of the mountain, beyond which the wave amplitude decays to less than  $0.01 \text{ m s}^{-1}$ . Vertical motion in the control run strongly resembles that in the  $L_v = 0$  run from 200 km upstream to 1000 km downstream of the ridge<sup>2</sup>. Further upstream (between  $x = -1000$  km and  $-200$  km), deep ascent is visible in the time-mean, suggesting that enhanced precipitation in this region is due to a feedback of moist convection on the mountain-induced low-level ascent. Lee waves are more prominent in the  $L_v = 0$  run, and  $w$  has slightly greater amplitude above the mountain, indicating higher flow nonlinearity in that run. This is consistent with the mountain wave in the control run experiencing a lower effective static stability due to latent heat release (see examples of Lalas and Einaudi (1973) for fully saturated atmospheres or Lapeyre and Held (2004) and O’Gorman (2011) for more general, unsaturated flows).

The similarity between the dry and moist  $w$  above the ridge raises the question of how much precipitation the dry wave would produce without moist convective feedback. The  $L_v = 0$  simulation does produce precipitation in its initial times, before moisture has been depleted (there are no surface fluxes in that run), though in a very different form (it is of stratiform type, and focused on the upwind slope only). Including this “dry mode precipitation” in the theory would require also decreasing

---

<sup>2</sup>A simple scale analysis explains the prominence of the “dry” gravity wave in the moist simulation. Dry vertical motion scales as  $w_{\text{dry}} \sim u_0 \frac{dh}{dx} \approx 0.15 \text{ m s}^{-1}$ , while the diabatic  $w$  scales as  $w_{\text{diabatic}} = Q_c / \frac{ds_0}{dz} = (gP/p_T)/(T_r N^2/g) \approx 0.024 \text{ m s}^{-1}$ , using  $P = 20 \text{ mm day}^{-1}$  (multiplied by  $\rho_w L_v$ ),  $T_r = c_p \times 300 \text{ K}$  and  $N = 0.01 \text{ s}^{-1}$ . Hence, gravity wave dynamics are expected to dominate over the ridge unless time-mean  $P$  increases by an order of magnitude.

$q_{dL}$ , which would have a compensating effect on the moist mode, leaving total precipitation nearly unchanged.

To illustrate the dynamics producing rainfall over the ridge, we plot the instantaneous vertical velocity at 500 hPa at a rainy time in Figure 5. Vertical motion over the upwind slope is composed of isolated deep convective cells (extending to 200 hPa, not shown) surrounded by cold pools, qualitatively similar to cells observed upstream over ocean. This justifies our approach of developing a theory for orographic precipitation based on the behavior of an ensemble of convective motions. Past the mountaintop, convective motions are absent, consistent with the lack of precipitation there.

#### *d. Thermodynamic equation*

We now evaluate the degree to which the linearization we employed as our starting point in (1a)-(1b), as well as WTG, are valid approximations.

Figure 6a shows vertically averaged terms from the thermodynamic equation (A1a) and its linearized version (1a), computed using time and meridional mean quantities (denoted with an overbar). Diabatic heating is computed as a residual and plotted with precipitation (or rather  $gP/p_T$ ) for comparison. The diagnosed diabatic heating underestimates precipitation immediately downstream of its peak, but shows very good agreement upstream. The linearized terms (i.e., replacing  $\mathbf{u}$  and  $s$  by  $\mathbf{u}_0$  and  $s_0$ ) closely match the “full” terms except between 30 km upstream to 100 km downstream of the peak. Much of the precipitation is concentrated upwind of this region, where it is accurately matched by the diabatic heating diagnosed from linearized terms. Between  $x = -30$  km and  $x = +100$  km, the small diabatic heating indicates that the disagreement between linearized and full terms is unlikely to be due to moist effects, and rather due to the nonlinear part of the dry mountain wave.

We now turn to validation of the WTG assumption. The good match between linearized temperature advection terms from the  $h_0 = 1000$  m simulation (i.e.,  $\langle \mathbf{u}_0 \cdot \nabla (\overline{T_d + T_m}) \rangle$ ) and from the  $L_v = 0$  simulation ( $\langle \mathbf{u}_0 \cdot \nabla \overline{T_d} \rangle$ ), shown in Figure 6b, ensures that  $|\mathbf{u}_0 \cdot \nabla T_m| \ll |\mathbf{u}_0 \cdot \nabla T_d|$ . The smallness of the dry residual  $\langle \mathbf{u}_0 \cdot \nabla \overline{T_d} + \overline{\omega_d} ds_0/dp \rangle$  indicates that the dry linearized thermodynamic budget holds. Taken together, these indicate that  $\langle \overline{\omega_m} ds_0/dp \rangle \simeq \langle \overline{Q_c} \rangle + \langle \overline{R} \rangle$ , which is exactly the WTG approximation.

#### 4. Comparing theory and simulations

Precipitation profiles from the convection-permitting numerical simulations are now used as a first test of our theory. We compare these profiles against both the linear theory (13) and the nonlinear one (7), with the dry forcing for the latter extracted from the simulations. We will show that while precipitation profiles are well-captured by the theory, their upstream amplitude is overestimated. This issue is addressed by modifying the adjustment time scales to values appropriate for seasonal means. A last adjustment incorporates the downstream modulation of surface evaporation and radiative cooling to (7).

##### a. Temperature and moisture deviations; validity of QE

We first examine lower-tropospheric temperature and moisture perturbations of the dry mode, which drive convection in (7), and compare these to predictions of the linear theory (obtained by combining (8) and (12)).

Figure 7a, b shows  $T'_L$  and  $q'_L$  from the  $h_0 = 1000$  m control and  $L_v = 0$  runs. These are time-averaged, meridional-averaged, and pressure-averaged (875 hPa to 700 hPa) deviations from a mean sounding 3000 km upstream of the mountaintop. Under our WTG assumptions,  $T'_L = T_{dL}$ , so we also plot  $T_{dL}$  as predicted by linear mountain wave theory with  $N = 0.01$  s<sup>-1</sup>. The agreement

is generally good, especially given our neglect of nonlinearity of the dry mountain wave, shown to be important above the peak in Figure 6. However, upstream of the mountain,  $T'_L$  in the control run is about a third smaller in magnitude than in the  $L_v = 0$  run, which is consistent with the dry mode feeling a reduced static stability in the control run with latent heat release (see section 3c). Including this effect in the theory would challenge our assumption that the dry mode is unaffected by the moist mode, and is left as potential improvement for future work.

An equally important modulator of convection is  $q'_L$ , which is shown in Figure 7b. We do not expect the control and  $L_v = 0$  runs to produce similar distributions of  $q_L$ :  $q_{mL}$  is expected, upstream, to be reduced by the precipitation forced by the dry mode, which happens as expected. Linear theory (with the same moisture lapse rate as in section 2d) matches  $q_{dL}$  estimated from the  $L_v = 0$  run upstream of the mountain peak (except its peak value is too high), and overestimates orographic wave-induced drying downstream. Moisture depletion at the beginning of the dry run (see section 3c) may explain this discrepancy, as  $q_{dL}$  is evaluated from the last 50 days of the  $L_v = 0$  run.

Altogether, these results suggest that linear theory (13) will estimate upstream distribution of precipitation nearly as accurately as the nonlinear theory (7) forced by the simulated  $q_{dL}$  and  $T_{dL}$ . One might expect the linear theory to yield a higher magnitude, due to an overestimated temperature decrease, if a reduced effective static stability is not used. Several elements are expected to affect predictions of the linear theory in the rain shadow: the overestimated subsidence-induced drying, and the neglect of the constraint that convective heating be non-negative.

The thermodynamic perturbations displayed in Figure 7a, b also allow evaluation of the validity of the QE hypothesis, which is often expressed as

$$\delta\theta_{e,b} \propto \delta\theta_e^*(p) \quad (21)$$

where  $\theta_{e,b}$  is the equivalent potential temperature below cloud base,  $\theta_e^*(p)$  is the saturation equivalent potential temperature at a level that is in QE with sub-cloud base air, and  $\delta$  expresses a variation in space or time (e.g. Emanuel et al. 1994). Past observational tests of QE have assessed these variations, evaluating them only in regions where convection is not suppressed and vertically averaging the right-hand side of (21) over the layer of interest (e.g. Brown and Bretherton 1997). Figure 7c shows time-mean horizontal deviations of  $\theta_{e,b}$  (averaged over the bottom three terrain-following levels, from approximately 70 m to 400 m above the surface) and  $\theta_e^*$  (averaged over our standard lower-tropospheric layer and hence denoted  $\theta_{e,L}^*$ ) from their far upstream values. Upwind of the mountain to the location of the peak precipitation, the decrease in  $\theta_{e,b}$  is commensurate with that in  $\theta_{e,L}^*$ , indicating that QE holds to a good approximation there. Between the mountaintop and  $x = 1000$  km, where convection is suppressed (gray shaded region in Fig. 3c), one does not expect QE to hold, and  $\theta_{e,b}$  is greatly reduced compared to  $\theta_{e,L}^*$ ; the two variables then converge as convective activity is recovered farther downstream.

Although this correspondence between variations in  $\theta_{e,b}$  and  $\theta_{e,L}^*$  in convecting regions indicates that a lower-tropospheric QE relation holds in the time mean in our simulations, it also seems worthwhile to discuss some relevant time scales. QE is based on the idea that the evolution of the forcing (here, cooling and moistening of the lower troposphere by the orographic wave) occurs on time scales much longer than those of the convective response. In an Eulerian framework, the orographic mechanical forcing is steady and we are concerned with the time mean response, so the time scales of the forcing and convective response are extremely well separated. One could, however, take a Lagrangian view in which air columns are advected by the mean wind toward the mountain, so the forcing evolves on a time scale  $l/u_0$ , about 7 hours if  $l$  is the  $e$ -folding length scale of perturbations upstream of the mountain (about 250 km). That time scale is not well-separated from the convective response time of order 2 to 3 hours (e.g., Tulich and Mapes 2010; Ahmed

et al. 2020). However, similarly rapid transport of air masses into the region of precipitating large-scale ascent occurs in disturbances that QE is often used to describe, such as the Madden-Julian Oscillation (Madden and Julian 1971; Haertel et al. 2017) and tropical cyclones (Emanuel 2007). In such disturbances and in our orographic forcing, QE is not being used to describe a single Lagrangian event, but the mean of a large ensemble of such events. In an Eulerian framework, such a system would be described by a fixed column subject to a steady advective tendency, with the large-scale forcing evolving on long, seasonal time scales.

### *b. Precipitation from prior theories*

Before comparing the simulated mean rainfall to the theory developed in section 2, we evaluate the performance of two well-known theories for mechanically forced orographic precipitation: the “upslope” model (see e.g. Roe 2005) and the linear theory of SB04. Both assume that condensation occurs due to upward motion in a saturated layer. The upslope model assumes terrain-parallel flow at all levels, while SB04 use linear mountain wave theory to solve for  $w$ . The latter model specifies time scales for the conversion of condensed water to raindrops and subsequent fallout.

With the topographic shape defined in (20), terrain-parallel flow produces ascent over the upwind slope only, and downward motion over the lee slope only. This renders the upslope model incapable of capturing any precipitation enhancement upstream of  $x = -100$  km, and any rain shadow downstream of  $x = -100$  km. It predicts peak precipitation of around  $450 \text{ mm day}^{-1}$ , an order of magnitude larger than the simulated value. We do not plot profiles from the upslope model because of this poor fit.

Although convection is not specifically represented in the SB04 model, latent heating is taken into account by using the moist Brunt-Väisälä frequency,  $N_m$ , as a measure of flow stability. However this quantity is imaginary in the present case as the flow is potentially unstable in the

lower troposphere, with  $\gamma > \Gamma_m$ , where  $\gamma = -dT/dz$  (resp.  $\Gamma_m$ ) is the environmental (resp. moist-adiabatic) lapse rate. Because of the similarity of the ascent patterns with and without latent heating (see Figure 4), we choose to use SB04's model by replacing  $N_m$  with  $N$ .

Because this theory assumes saturated flow, it is expected to overestimate precipitation if non-precipitating times are not accounted for. So we compute the time- and meridional-mean rain rate excluding non-precipitating times (Appendix B provides details), which roughly doubles  $P'$  (i.e.  $P_{1000} - P_0$ ) compared to the full time-mean. This suggests the SB04 prediction of  $P'$  should be divided by 2, but a better fit to the WRF simulation is obtained when dividing  $P'$  by 2.5 (green line in Figure 8a). We used conversion and fallout times of 2000 s,  $P_0 = 4.5 \text{ mm day}^{-1}$ ,  $\Gamma_m = 4.3 \text{ K/km}$ ,  $\gamma = 5 \text{ K/km}$  and  $N = 0.012 \text{ s}^{-1}$ .

While the SB04 theory captures the general shape of precipitation upstream of the mountain, it underestimates its upstream extent. But its largest bias lies in the lee, where instead of reproducing the simulation's long rain shadow, it predicts a strong secondary precipitation maximum due to the mountain wave ascent there. Hence, although the SB04 model is regarded as a skillful predictor of midlatitude orographic precipitation, it has important deficiencies for this case of tropical deep convective rainfall.

### *c. Precipitation from the present theory*

We now assess the linear theory (13). Applying it with the same parameters used in section 2d overestimates the unconditional time-mean peak precipitation in the WRF simulation by a factor of two to three (not shown), as occurred for the SB04 theory. We hypothesize that this occurs because increased adjustment time scales ( $\tau_q$  and  $\tau_T$ ) are needed when applying the theory to seasonal-scale time means. Spatio-temporal averaging of the convective heating term (3) necessarily includes non-convective regions and times, yielding higher effective adjustment scales (Ahmed et al. 2020).

The theoretical  $P'$  is, in the upstream region, inversely proportional to the adjustment scales because (7) is linear in that region where  $P > 0$ . This suggests that accounting for non-precipitating times requires increasing  $\tau_q$  and  $\tau_T$ , compared to the “instantaneous” values estimated by Ahmed et al. (2020). The simulated mean precipitation is best fit by increasing both adjustment times 2.5-fold (yielding  $\tau_T = 7.5$  hours and  $\tau_q = 27.5$  hours), near the factor of 2 expected from excluding non-precipitating times from the time-average (see above and Appendix B).

Figure 8b displays the application of (13) to the mountain profile (20) used in the simulations, with  $h_0 = 1000$  m (Fig. 8c shows the same for  $h_0 = 500$  m). We set  $P_0 = 4.5 \text{ mm day}^{-1}$  to match the simulations (see section 3b). We use the same values of  $dq_0/dz$  and  $ds_0/dz$  as in section 2d, and we keep  $M/M_S = 0.2$  henceforth<sup>3</sup>. Linear theory overestimates the peak precipitation on the upwind flank of the ridge. The fit might be improved by accounting for a lower effective static stability (as explained in section 4a), but we did not attempt this. Note that without adjusting the time scales, it would be substantially higher than what the linear theory produced for the Witch of Agnesi profile (Figure 2) because of the steeper ascent imposed by (20). A more gradual ascent provides a greater distance for  $P$  to relax back to  $P_0$  (first term on the right-hand side of (7)).

As an intermediate level of complexity between linear theory and the convection-permitting simulations, Figures 8b, c display mean precipitation computed from the general precipitation equation (7). This required estimating the dry forcings  $T_{dL}$  and  $q_{dL}$ .  $T_{dL}$  was estimated from the  $h_0 = 1000$  m and  $h_0 = 500$  m simulations. We did not take it from the  $L_v = 0$  run because we suspect the dry mode in that simulation behaves differently due to a higher effective static stability than in the control run (see sections 3c and 4a); using a more accurate estimate offers a better test of the theory. We estimated  $q_{dL}$  from the  $L_v = 0$  simulation (we used half this value for the

---

<sup>3</sup>Indeed, following the method outlined by Yu et al. (1998), we estimate  $M_s = 2370 \text{ J kg}^{-1}$  and  $M_h = 455 \text{ J kg}^{-1}$  in the  $h_0 = 1000$  m run (respectively  $2341 \text{ J kg}^{-1}$  and  $450 \text{ J kg}^{-1}$  in the  $h_0 = 500$  m run).

$h_0 = 500$  m run, due to the absence of an  $h_0 = 500$  m,  $L_v = 0$  run), because it cannot be directly estimated from the control simulation due to the moist and dry mode both contributing to specific humidity anomalies (see section 4a). Downstream of the mountain,  $q_{dL}$  oscillates in a way not seen in the dry mode of the control run (owing to the smaller amplitude of the orographic lee wave, see Figure 4), but we did not correct for this. All other parameters are the same as above, and (7) is integrated numerically with a backward differentiation formula method. As expected from the profiles in Figure 7a, b, precipitation computed this way compares well with linear theory, except for a peak that is smaller and shifted modestly downstream, hence closer to the simulated rainfall.

Two effects explain the differences between precipitation rates computed from our general precipitation equation (7) and our linear theory (13) downstream of the mountain. First, oscillations in the precipitation rate, including a weak local maximum between 400 km and 600 km downwind of the mountain peak, are due to the shapes of  $q_{dL}$  and  $T_{dL}$  in the convection-permitting simulations. Second, the Heaviside function in (7) increases the length of non-precipitating regions; forbidding negative values of  $P$  reduces the recovery rate  $(P_0 - P)/L_q$ , so that  $P$  converges towards  $P_0$  more slowly.

#### *d. Surface evaporation and radiative cooling in the rain shadow*

Using the nonlinear theory with increased time scales overestimates the simulated precipitation downstream of the mountain (Figure 8b, c), possibly because the theory neglects variations in surface latent heat fluxes and radiative cooling (i.e., it assumes  $P_0$  is uniform). Profiles of  $\langle E \rangle$ ,  $\langle R \rangle$ , and the surface sensible heat flux are shown in Figure 9a.

The starker deviations from the constant upstream values occur above the mountain and 100 km to 2000 km downwind of the mountaintop. A strong reduction in surface evaporation above the ridge, which is covered with land, is largely compensated by increased sensible heating.

Downstream, surface evaporation increases over a 200 km-long region before decreasing to 80% of its upstream value. This decrease in the region  $x > 200$  km can be attributed (not shown) to increased near-surface relative humidity, likely caused by suppressed convection in that region. Suppressed convection also reduces the occurrence of high clouds and, as a consequence, increases radiative cooling by up to 10% downstream. Earlier theory (e.g. Fuchs and Raymond 2002) parameterized this effect with a feedback factor, setting  $\langle R \rangle'$  proportional to  $P'$  (where  $\langle R \rangle'$  denotes radiative cooling minus its RCE value).

The downstream modulation of  $\langle E \rangle$  and  $\langle R \rangle$  strongly decreases  $P_0$ , according to (6). Accounting for this in (7) nearly halves the computed rain rate downstream, as shown in Figure 9b. Incorporating a closure for  $\langle E \rangle$  and  $\langle R \rangle$  into our theory, rather than diagnosing these from simulations, is left for future work.

## 5. Summary and conclusions

We present a theory of convective precipitation forced by the mechanical effects of orography at low latitudes. It starts with decomposition of the flow into the sum of a dry mode, carrying the orographic gravity wave, and a moist mode bearing the convective response. Precipitation is assumed to be produced entirely by the moist mode, whose dynamics are vertically truncated and subject to the WTG approximation. Convective heating responds to lower-tropospheric temperature and moisture perturbations carried by both modes in a quasi-equilibrium framework. Two degrees of complexity can be employed. The first consists of computing the dry mode perturbations with a numerical model for use in the theory, with the theory retaining the nonlinearity of the convective closure. The second option neglects this nonlinearity and assumes linear mountain wave dynamics to derive a linear model of convective orographic rainfall much in the spirit of the SB04 midlatitude model. The linear theory provides analytical solutions to probe the sensitivity

of maximum precipitation, upstream extent of precipitation enhancement, and rain-shadow length to the physical parameters at play, namely upstream wind, convective adjustment scales, relative GMS, static stability, and moisture lapse rate.

This theory describes time-mean rainfall in tropical orographic regions, and assumptions related to the vertical structure of the moist mode and WTG prevent its use in midlatitudes. Its applicability to short-term precipitating events is also questionable, owing to the unsuitability of the QE assumption at these time scales. It does not account for cloud delays nor the advection of hydrometeors, although we believe these could be added to the linear version without much difficulty. Most importantly, the model is not suited to the description of thermally forced orographic convection.

The theory is tested against convection-permitting simulations in long-channel geometry. The dry orographic gravity wave is prominent in the moist model, justifying its consideration as a driver of terrain-generated convection. After correcting adjustment time scales to account for the effects of seasonal averaging, the theory accurately reproduces precipitation rates simulated by this model, especially upstream of the mountain peak. The linear version is skillful at modeling dry temperature and moisture deviations, and hence precipitation, upwind of the ridge. The mountain alters surface evaporation and radiative cooling far downstream, reducing rainfall there. We note that the nondimensional mountain heights considered here avoid strongly nonlinear flows; testing the theory in such cases is left for future work.

This theory is envisioned as a tool for understanding the spatial variability of rainfall in tropical orographic regions where mechanical forcing prevails. Examples include South Asia and Mexico during their respective summer monsoons, or most tropical land regions subject to an autumn monsoon (Ramesh et al. 2021). Understanding the interaction of large-scale flow with orography in such regions is key to comprehending past variability in tropical rainfall, as well as predicting

changes in coming decades. The theory could also be used to probe the importance of orography in shaping large-scale tropical circulations through its influence on moist convection.

*Acknowledgments.* This material is based on work supported by the U.S. Department of Energy, Office of Science, Office of Biological and Environmental Research, Climate and Environmental Sciences Division, Regional and Global Model Analysis Program, under Award DE-SC0019367. It used resources of the National Energy Research Scientific Computing Center (NERSC), which is a DOE Office of Science User Facility. QN acknowledges support from the McQuown fund at UC Berkeley. The authors wish to thank Daniel Kirshbaum for very helpful feedback and suggestions.

*Data availability statement.* Processed WRF output and code used in producing the figures will be archived at Zenodo, with a DOI issued once the review process and any needed revisions are complete. Raw WRF output is available from the authors upon request ([qnicolas@berkeley.edu](mailto:qnicolas@berkeley.edu)), and GPM IMERG and ERA5 data are publicly accessible online.

## APPENDIX A

### Decomposition into dry and moist modes

We describe flow over a tropical mountain as the sum of a dry mode (representing the influence of orography in the absence of condensation) and a moist convective one. The dry mode affects the moist mode through convective heating, but the moist mode does not feed back on the dry mode. Steady-state thermodynamic and moisture equations are

$$\mathbf{u} \cdot \nabla T + \omega \frac{\partial s}{\partial p} = Q_c - R, \quad (\text{A1a})$$

$$\mathbf{u} \cdot \nabla q + \omega \frac{\partial q}{\partial p} = Q_q + E, \quad (\text{A1b})$$

with notation as in section 2a. Wind, moisture and temperature are decomposed as follows:

$$\begin{aligned}
\omega &= 0 + \omega_d + \omega_m, \\
\mathbf{u} &= \mathbf{u}_0 + \mathbf{u}_d + \mathbf{u}_m, \\
q &= q_0(p) + q_d + q_m, \\
T &= T_0(p) + T_d + T_m,
\end{aligned} \tag{A2}$$

where subscripts  $d$  and  $m$  denote dry and moist modes, respectively.

We now linearize (A1a)-(A1b) about a state of uniform horizontal wind  $\mathbf{u}_0$ , zero vertical velocity, and horizontally uniform dry static energy  $s_0(p)$  and specific humidity  $q_0(p)$ . We justify this approach based on scales estimated from the  $h_0 = 1000$  m control and  $L_v = 0$  simulations. For horizontal advection terms, the assumption  $|\mathbf{u}_m| \ll |\mathbf{u}_0|$  is well justified as the standard deviation of  $\mathbf{u}$  is less than  $2 \text{ m s}^{-1}$  in the RCE region of our convection-permitting simulations. The dry mode, on the contrary, is expected to be nonlinear, as  $|\mathbf{u}_d|/|\mathbf{u}_0| \simeq Nh_0/u_0$ . Nevertheless, we find in the simulations that  $|\mathbf{u}_d| \ll 0.3|\mathbf{u}_0|$  everywhere except right above the mountain. In section 3d, we show that such nonlinearity in the dry dynamics does not seem to affect the moist mode dynamics, despite its local importance in the thermodynamic budget.

For vertical advection terms, we assume  $\partial s_d/\partial p, \partial s_m/\partial p \ll \partial s_0/\partial p$ , with a similar treatment for moisture stratification. Again, this is supported by the simulations except for the dry perturbations right above the mountain. In height coordinates,  $\partial s_0/\partial z \simeq 4 \text{ K/km}$ , and deviations above the mountain in the  $L_v = 0$  simulation give  $|\partial s_d/\partial z| \lesssim 1 - 2 \text{ K/km}$ . Static stability variations from the moist mode are at least two orders of magnitude smaller than the basic state static stability (see Neelin and Zeng 2000).

Using these approximations, (A1a)-(A1b) become

$$\mathbf{u}_0 \cdot \nabla T_d + \omega_d \frac{\partial s_0}{\partial p} + \mathbf{u}_0 \cdot \nabla T_m + \omega_m \frac{\partial s_0}{\partial p} = Q_c - R, \quad (\text{A3a})$$

$$\mathbf{u}_0 \cdot \nabla q_d + \omega_d \frac{\partial q_0}{\partial p} + \mathbf{u}_0 \cdot \nabla q_m + \omega_m \frac{\partial q_0}{\partial p} = Q_q + E. \quad (\text{A3b})$$

The first two terms in each equation (the dry mode) balance each other, expressing conservation of potential temperature and moisture in the dry perturbation. Note that  $Q_q$  could potentially be nonzero in the dry mode (i.e., some moisture could condense and fall, even in the absence of latent heating), but this effect is confined to the upwind mountain slope in the  $L_v = 0$  run (consistently with Zhang and Smith (2018)); further discussion is provided in section 3c. Accounting for the dry mode balance in (A3a)-(A3b) yields (1a)-(1b).

## APPENDIX B

### Selection of precipitating times

To justify the increase in adjustment time scales needed to represent seasonal-mean dynamics, we show how the exclusion of non-precipitating times leads to a doubling of the time-mean rain rate. Rainfall in the  $h_0 = 1000$  m and 500 m simulations is produced by a variety of convective systems (e.g. Figure 5) propagating near velocity  $\mathbf{u}_0$ . Figure B1a shows a Hovmöller diagram of meridionally averaged precipitation over days 175-200 in the  $h_0 = 1000$  m simulation. We average precipitation over characteristic lines  $L_t = (t, x(t) = x_0 + u_0 t)$  with  $x_0 = -4905$  km and  $t$  running from days 50 to 188 (the last time for which the whole characteristic line is included in the domain) in hourly samples. The resulting  $P_{\text{characteristic}}(L_t)$  is plotted for days 175-188 in Figure B1b. The mean rainfall over precipitating times,  $P_{\text{precipitating}}$ , is then computed as the average over characteristic lines satisfying  $P_{\text{characteristic}} > 2 \text{ mm day}^{-1}$ . It is displayed in figure B2, along with the all-time mean  $P_{1000}$ .

## References

- Abramowitz, M., and I. A. Stegun, 1964: *Handbook of Mathematical Functions with Formulas, Graphs, and Mathematical Tables*. ninth dover printing, tenth gpo printing ed., Dover, New York City.
- Ahmed, F., Á. F. Adames, and J. D. Neelin, 2020: Deep convective adjustment of temperature and moisture. *Journal of the Atmospheric Sciences*, **77** (6), 2163 – 2186, doi: 10.1175/JAS-D-19-0227.1.
- Arakawa, A., and W. H. Schubert, 1974: Interaction of a cumulus cloud ensemble with the large-scale environment, part I. *Journal of Atmospheric Sciences*, **31** (3), 674 – 701, doi: 10.1175/1520-0469(1974)031<0674:IOACCE>2.0.CO;2.
- Biasutti, M., S. E. Yuter, C. D. Burleyson, and A. H. Sobel, 2012: Very high resolution rainfall patterns measured by TRMM precipitation radar: seasonal and diurnal cycles. *Climate Dynamics*, **39** (1), 239–258.
- Brown, R. G., and C. S. Bretherton, 1997: A test of the strict quasi-equilibrium theory on long time and space scales. *Journal of the Atmospheric Sciences*, **54** (5), 624 – 638.
- Cannon, D. J., D. J. Kirshbaum, and S. L. Gray, 2014: A mixed-phase bulk orographic precipitation model with embedded convection. *Quarterly Journal of the Royal Meteorological Society*, **140** (683), 1997–2012, doi:10.1002/qj.2269.
- Chen, S.-H., and Y.-L. Lin, 2005: Effects of moist Froude number and CAPE on a conditionally unstable flow over a mesoscale mountain ridge. *Journal of the Atmospheric Sciences*, **62** (2), 331 – 350, doi:10.1175/JAS-3380.1.

Chu, C.-M., and Y.-L. Lin, 2000: Effects of orography on the generation and propagation of mesoscale convective systems in a two-dimensional conditionally unstable flow. *Journal of the Atmospheric Sciences*, **57** (23), 3817 – 3837, doi:10.1175/1520-0469(2001)057<3817:EOOOTG>2.0.CO;2.

Derbyshire, S. H., I. Beau, P. Bechtold, J.-Y. Grandpeix, J.-M. Piriou, J.-L. Redelsperger, and P. M. M. Soares, 2004: Sensitivity of moist convection to environmental humidity. *Quarterly Journal of the Royal Meteorological Society*, **130** (604), 3055–3079, doi:10.1256/qj.03.130.

Derin, Y., and Coauthors, 2019: Evaluation of GPM-era global satellite precipitation products over multiple complex terrain regions. *Remote Sensing*, **11** (24).

Durran, D. R., 2003: Lee waves and mountain waves. *Encyclopedia of atmospheric sciences*, **1161**, 1170.

Emanuel, K. A., 2007: Quasi-equilibrium dynamics of the tropical atmosphere. *The Global Circulation of the Atmosphere*, T. Schneider, and A. H. Sobel, Eds., Princeton University Press, 186–218.

Emanuel, K. A., J. David Neelin, and C. S. Bretherton, 1994: On large-scale circulations in convecting atmospheres. *Quarterly Journal of the Royal Meteorological Society*, **120** (519), 1111–1143, doi:10.1002/qj.49712051902.

Epifanio, C. C., and D. R. Durran, 2001: Three-dimensional effects in high-drag-state flows over long ridges. *Journal of the Atmospheric Sciences*, **58** (9), 1051 – 1065.

Fuchs, Ž., and D. Raymond, 2002: Large-scale modes of a nonrotating atmosphere with water vapor and cloud–radiation feedbacks. *Journal of the Atmospheric Sciences*, **59**, 1669–1679.

Haertel, P., W. R. Boos, and K. Straub, 2017: Origins of moist air in global lagrangian simulations of the Madden–Julian oscillation. *Atmosphere*, **8** (9).

Hersbach, H., and Coauthors, 2020: The ERA5 global reanalysis. *Quarterly Journal of the Royal Meteorological Society*, **146** (730), 1999–2049, doi:10.1002/qj.3803.

Houze, R. A., 2012: Orographic effects on precipitating clouds. *Reviews of Geophysics*, **50** (1), doi:10.1029/2011RG000365.

Houze, R. A., K. L. Rasmussen, M. D. Zuluaga, and S. R. Brodzik, 2015: The variable nature of convection in the tropics and subtropics: A legacy of 16 years of the Tropical Rainfall Measuring Mission satellite. *Reviews of Geophysics*, **53** (3), 994–1021.

Huffman, G. J., and Coauthors, 2019: NASA Global Precipitation Measurement (GPM) Integrated Multi-Satellite Retrievals for GPM (IMERG). NASA Algorithm Theoretical Basis Doc., Version 06. 38 pp.

Iacono, M. J., J. S. Delamere, E. J. Mlawer, M. W. Shephard, S. A. Clough, and W. D. Collins, 2008: Radiative forcing by long-lived greenhouse gases: Calculations with the AER radiative transfer models. *Journal of Geophysical Research: Atmospheres*, **113** (D13), doi:10.1029/2008JD009944.

Janjić, Z., 2002: Nonsingular implementation of the Mellor–Yamada level 2.5 scheme in the NCEP Meso model. *NCEP Office Note*, **436**.

Jiménez, P. A., J. Dudhia, J. F. González-Rouco, J. Navarro, J. P. Montávez, and E. García-Bustamante, 2012: A revised scheme for the WRF surface layer formulation. *Monthly Weather Review*, **140** (3), 898 – 918, doi:10.1175/MWR-D-11-00056.1.

Kirshbaum, D. J., 2020: Numerical simulations of orographic convection across multiple gray zones. *Journal of the Atmospheric Sciences*, **77** (10), 3301 – 3320, doi:10.1175/JAS-D-20-0035.1.

Kirshbaum, D. J., B. Adler, N. Kalthoff, C. Barthlott, and S. Serafin, 2018: Moist orographic convection: Physical mechanisms and links to surface-exchange processes. *Atmosphere*, **9** (3), doi:10.3390/atmos9030080.

Kirshbaum, D. J., and R. B. Smith, 2009: Orographic precipitation in the tropics: Large-eddy simulations and theory. *Journal of the Atmospheric Sciences*, **66** (9), 2559 – 2578, doi:10.1175/2009JAS2990.1.

Lalas, D. P., and F. Einaudi, 1973: On the stability of a moist atmosphere in the presence of a background wind. *Journal of the Atmospheric Sciences*, **30**, 795–800.

Lapeyre, G., and I. M. Held, 2004: The role of moisture in the dynamics and energetics of turbulent baroclinic eddies. *Journal of the Atmospheric Sciences*, **61** (14), 1693 – 1710.

Madden, R. A., and P. R. Julian, 1971: Detection of a 40–50 day oscillation in the zonal wind in the tropical Pacific. *Journal of Atmospheric Sciences*, **28** (5), 702 – 708.

Mellor, G. L., and T. Yamada, 1982: Development of a turbulence closure model for geophysical fluid problems. *Reviews of Geophysics*, **20** (4), 851–875, doi:10.1029/RG020i004p00851.

Miglietta, M. M., and R. Rotunno, 2009: Numerical simulations of conditionally unstable flows over a mountain ridge. *Journal of the Atmospheric Sciences*, **66** (7), 1865 – 1885, doi:10.1175/2009JAS2902.1.

Miglietta, M. M., and R. Rotunno, 2012: Application of theory to simulations of observed cases of orographically forced convective rainfall. *Monthly Weather Review*, **140** (9), 3039 – 3053, doi:10.1175/MWR-D-11-00253.1.

Miglietta, M. M., and R. Rotunno, 2014: Numerical simulations of sheared conditionally unstable flows over a mountain ridge. *Journal of the Atmospheric Sciences*, **71** (5), 1747 – 1762, doi: 10.1175/JAS-D-13-0297.1.

Neelin, J. D., and I. M. Held, 1987: Modeling tropical convergence based on the moist static energy budget. *Monthly Weather Review*, **115** (1), 3 – 12.

Neelin, J. D., and N. Zeng, 2000: A quasi-equilibrium tropical circulation model—formulation. *Journal of the Atmospheric Sciences*, **57** (11), 1741 – 1766, doi:10.1175/1520-0469(2000)057<1741:AQETCM>2.0.CO;2.

Neiman, P. J., M. Hughes, B. J. Moore, F. M. Ralph, and E. M. Sukovich, 2013: Sierra barrier jets, atmospheric rivers, and precipitation characteristics in northern California: A composite perspective based on a network of wind profilers. *Monthly Weather Review*, **141** (12), 4211 – 4233, doi:10.1175/MWR-D-13-00112.1.

Nie, J., W. R. Boos, and Z. Kuang, 2010: Observational evaluation of a convective quasi-equilibrium view of monsoons. *Journal of Climate*, **23** (16), 4416–4428.

Niu, G.-Y., and Coauthors, 2011: The community Noah land surface model with multiparameterization options (Noah-MP): 1. model description and evaluation with local-scale measurements. *Journal of Geophysical Research: Atmospheres*, **116** (D12), doi:10.1029/2010JD015139.

O’Gorman, P. A., 2011: The effective static stability experienced by eddies in a moist atmosphere. *Journal of the Atmospheric Sciences*, **68** (1), 75 – 90, doi:10.1175/2010JAS3537.1.

Pierrehumbert, R. T., and B. Wyman, 1985: Upstream effects of mesoscale mountains. *Journal of the Atmospheric Sciences*, **42** (10), 977–1003.

Queney, P., 1948: The problem of air flow over mountains: A summary of theoretical studies. *Bulletin of the American Meteorological Society*, **29** (1), 16 – 26, doi:10.1175/1520-0477-29.1.16.

Ramesh, N., Q. Nicolas, and W. R. Boos, 2021: The globally coherent pattern of autumn monsoon precipitation. *Journal of Climate*, **34** (14), 5687 – 5705, doi:10.1175/JCLI-D-20-0740.1.

Raymond, D., Ž. Fuchs, S. Gjorgjevska, and S. Sessions, 2015: Balanced dynamics and convection in the tropical troposphere. *Journal of Advances in Modeling Earth Systems*, **7** (3), 1093–1116, doi:10.1002/2015MS000467.

Raymond, D. J., S. L. Sessions, A. H. Sobel, and Ž. Fuchs, 2009: The mechanics of gross moist stability. *Journal of Advances in Modeling Earth Systems*, **1** (3).

Roe, G. H., 2005: Orographic precipitation. *Annual Review of Earth and Planetary Sciences*, **33** (1), 645–671, doi:10.1146/annurev.earth.33.092203.122541.

Satoh, M., B. Stevens, F. Judt, M. Khairoutdinov, S.-J. Lin, W. M. Putman, and P. Düben, 2019: Global cloud-resolving models. *Current Climate Change Reports*, **5** (3), 172–184.

Skamarock, C., and Coauthors, 2019: A description of the Advanced Research WRF model version 4. Note NCAR/TN-556+STR, 145 pp.

Smith, R., 1989: Hydrostatic airflow over mountains. *Advances in Geophysics*, **31**, 1–41.

Smith, R. B., 1979: The influence of mountains on the atmosphere. *Advances in Geophysics*, **21**, 87–230, doi:10.1016/S0065-2687(08)60262-9.

Smith, R. B., and I. Barstad, 2004: A linear theory of orographic precipitation. *Journal of the Atmospheric Sciences*, **61** (12), 1377 – 1391, doi:10.1175/1520-0469(2004)061<1377:ALTOOP>2.0.CO;2.

Sobel, A. H., J. Nilsson, and L. M. Polvani, 2001: The weak temperature gradient approximation and balanced tropical moisture waves. *Journal of the Atmospheric Sciences*, **58** (23), 3650 – 3665, doi:10.1175/1520-0469(2001)058<3650:TWTGAA>2.0.CO;2.

Tan, J., C. Jakob, and T. P. Lane, 2013: On the identification of the large-scale properties of tropical convection using cloud regimes. *Journal of Climate*, **26** (17), 6618 – 6632.

Thompson, G., P. R. Field, R. M. Rasmussen, and W. D. Hall, 2008: Explicit forecasts of winter precipitation using an improved bulk microphysics scheme. part II: Implementation of a new snow parameterization. *Monthly Weather Review*, **136** (12), 5095 – 5115, doi:10.1175/2008MWR2387.1.

Tulich, S. N., and B. E. Mapes, 2010: Transient environmental sensitivities of explicitly simulated tropical convection. *Journal of the Atmospheric Sciences*, **67** (4), 923 – 940.

Wang, S., and A. H. Sobel, 2017: Factors controlling rain on small tropical islands: Diurnal cycle, large-scale wind speed, and topography. *Journal of the Atmospheric Sciences*, **74** (11), 3515–3532.

Wing, A. A., and T. W. Cronin, 2016: Self-aggregation of convection in long channel geometry. *Quarterly Journal of the Royal Meteorological Society*, **142** (694), 1–15, doi:10.1002/qj.2628.

Xie, S.-P., H. Xu, N. H. Saji, Y. Wang, and W. T. Liu, 2006: Role of narrow mountains in large-scale organization of asian monsoon convection. *Journal of Climate*, **19** (14), 3420 – 3429, doi:10.1175/JCLI3777.1.

Yang, Z.-L., and Coauthors, 2011: The community Noah land surface model with multiparameterization options (Noah-MP): 2. evaluation over global river basins. *Journal of Geophysical Research: Atmospheres*, **116** (D12), doi:10.1029/2010JD015140.

Yu, J.-Y., C. Chou, and J. D. Neelin, 1998: Estimating the gross moist stability of the tropical atmosphere. *Journal of the Atmospheric Sciences*, **55** (8), 1354 – 1372, doi: 10.1175/1520-0469(1998)055<1354:ETGMSO>2.0.CO;2.

Zhang, G., and R. B. Smith, 2018: Numerical study of physical processes controlling summer precipitation over the Western Ghats region. *Journal of Climate*, **31** (8), 3099 – 3115, doi: 10.1175/JCLI-D-17-0002.1.

## LIST OF FIGURES

- Fig. 1.** Annual-mean GPM IMERG V06B precipitation (shading), 500 m surface height level (thin brown contours), and wind vectors 100 m above the surface averaged over (a) June-August and (b) October-December from 2014 to 2020. (c) Cross-sections of surface elevation and precipitation along the thick blue line shown on panels a and b at 15°N. . . . . 48
- Fig. 2.** Precipitation predicted by the linear theory (13) with a Witch-of-Agnesi mountain profile and varying mountain heights and adjustment time scales (solid lines). The dashed line shows the precipitation obtained when neglecting the damping term in (14), for the parameters given in the first line of the legend. The thin horizontal line shows the basic-state precipitation  $P_0$ . . . . . 49
- Fig. 3.** Time and meridional mean precipitation (a) and CAPE (b) in the  $h_0 = 500$  m and 1000 m runs. Thin horizontal lines indicate the upstream-averaged (between  $x = -2500$  km and -3000 km) values. The magenta line in panel a shows the result of doubling the orographically-modified part of the precipitation ( $P - P_0$ ) in the  $h_0 = 500$  m run. Shadings show the interquartile ranges, as computed from binning each quantity into meridional and 10-day means at each longitude. Note that the topographic shape is different here from the Witch-of-Agnesi used in Figure 2, which was employed for purposes of analytical tractability. . . . . 50
- Fig. 4.** Time and meridionally-averaged vertical velocities from the  $h_0 = 1000$  m control run (a) and  $L_v = 0$  run (b). Note the nonlinearity of the color scale. . . . . 51
- Fig. 5.** Instantaneous vertical velocity at 500 hPa in the vicinity of the mountain, from the  $h_0 = 1000$  m run, day 150, 19h. . . . . 52
- Fig. 6.** Vertically averaged thermodynamic budget terms. Panel a shows ‘full’ (nonlinear) terms for the  $h_0 = 1000$  m control run, as well as their linearized version (obtained by fixing  $\mathbf{u}$  and  $s$  to their basic state values). The simulated precipitation rate is shown in blue for comparison. Panel b focuses on the linearized heat advection and adiabatic cooling terms, comparing the  $h_0 = 1000$  m control and  $L_v = 0$  runs. The vertical black lines show the extent of the mountain. . . . . 53
- Fig. 7.** Profiles of lower-tropospheric averaged temperature (a) and moisture (b) perturbations relative to 3000 km upstream in the  $h_0 = 1000$  m control and  $L_v = 0$  simulations, as well as perturbations computed from the linear theory (8) and (12)). Panel c shows perturbations of lower-tropospheric averaged saturation equivalent potential temperature and boundary layer averaged equivalent potential temperature, in the  $h_0 = 1000$  m control run. Gray shading shows the convectively decoupled region where  $P_{1000} < 2 \text{ mm day}^{-1}$ . . . . . 54
- Fig. 8.** Profiles of mean precipitation rates over 1000 m high (a and b) and 500 m high (c) mountains. Solid lines are simulated rates, dashed lines are computed from the nonlinear theory (7) with lower-tropospheric perturbations  $q_{dL}$  and  $T_{dL}$  diagnosed from simulations (see text), and dotted lines are profiles from the closed linear theory (13). The convective adjustment scales are taken from Ahmed et al. (2020) (a), then increased 2.5-fold (b and c). The thin horizontal lines show  $P_0$ . . . . . 55
- Fig. 9.** (a) Time and meridionally averaged surface fluxes and radiative cooling from the  $h_0 = 1000$  m simulation. Thin horizontal lines indicate the upstream-averaged (between -2500 km and -3000 km) values. (b) As in Figure 8b,c, without solutions from (13), and where solutions from (7) take into account spatial variations in surface evaporation and radiative cooling. Compare the profiles between 1000 km and 2500 km downstream of the mountains. . . . . 56



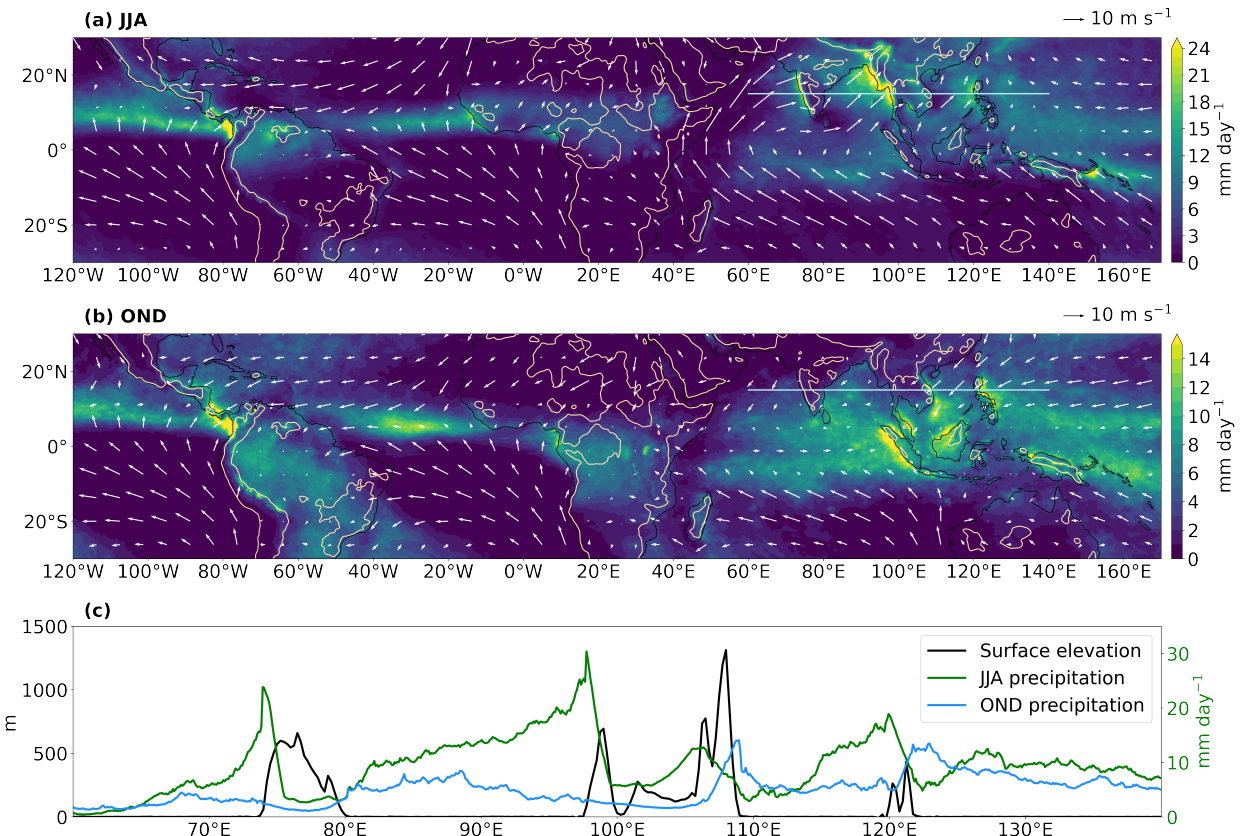


FIG. 1. Annual-mean GPM IMERG V06B precipitation (shading), 500 m surface height level (thin brown contours), and wind vectors 100 m above the surface averaged over (a) June-August and (b) October-December from 2014 to 2020. (c) Cross-sections of surface elevation and precipitation along the thick blue line shown on panels a and b at 15°N.

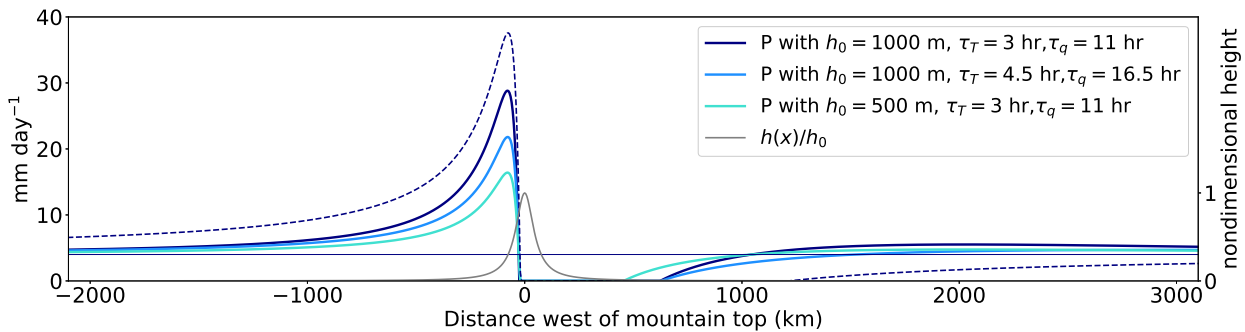


FIG. 2. Precipitation predicted by the linear theory (13) with a Witch-of-Agnesi mountain profile and varying mountain heights and adjustment time scales (solid lines). The dashed line shows the precipitation obtained when neglecting the damping term in (14), for the parameters given in the first line of the legend. The thin horizontal line shows the basic-state precipitation  $P_0$ .

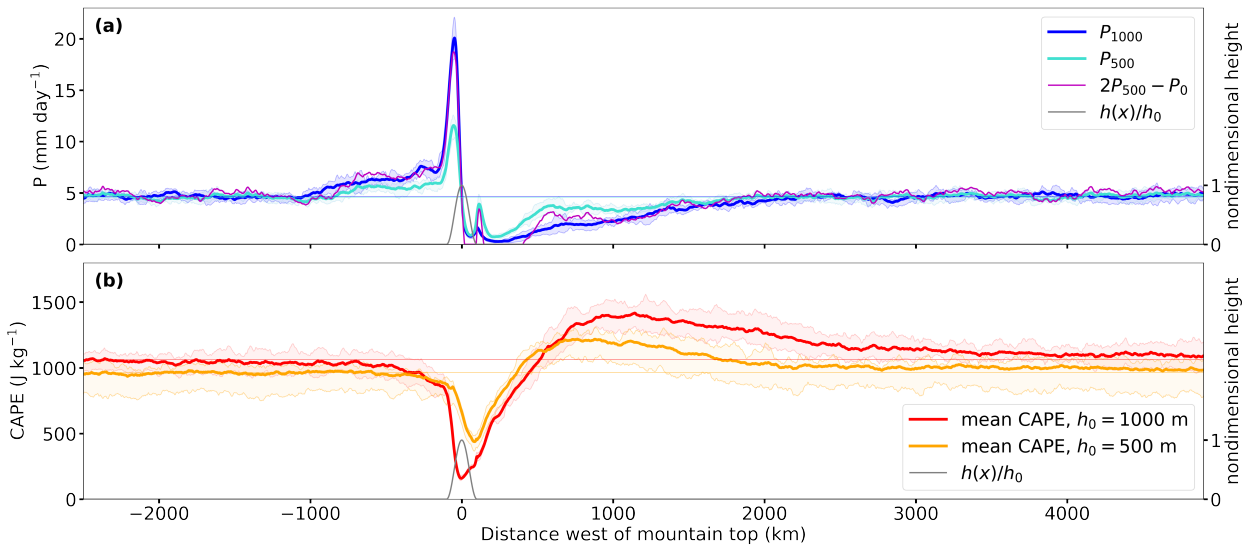


FIG. 3. Time and meridional mean precipitation (a) and CAPE (b) in the  $h_0 = 500 \text{ m}$  and  $1000 \text{ m}$  runs. Thin horizontal lines indicate the upstream-averaged (between  $x = -2500 \text{ km}$  and  $-3000 \text{ km}$ ) values. The magenta line in panel a shows the result of doubling the orographically-modified part of the precipitation ( $P - P_0$ ) in the  $h_0 = 500 \text{ m}$  run. Shadings show the interquartile ranges, as computed from binning each quantity into meridional and 10-day means at each longitude. Note that the topographic shape is different here from the Witch-of-Agnesi used in Figure 2, which was employed for purposes of analytical tractability.

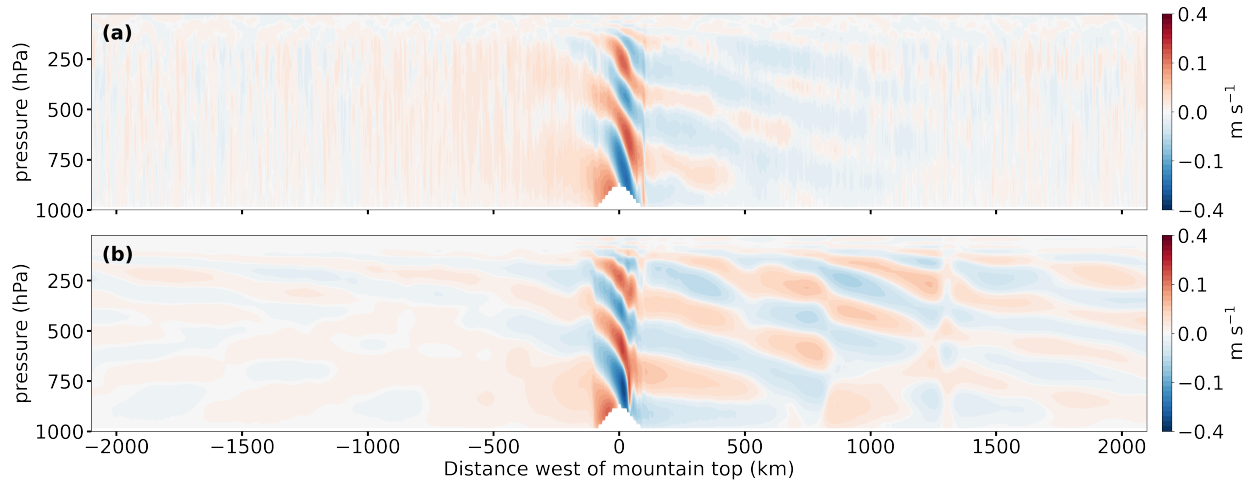


FIG. 4. Time and meridionally-averaged vertical velocities from the  $h_0 = 1000$  m control run (a) and  $L_v = 0$  run (b). Note the nonlinearity of the color scale.

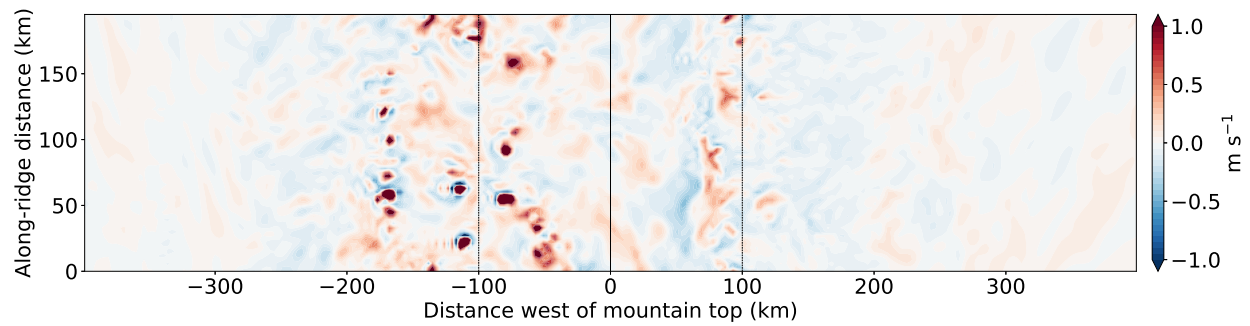


FIG. 5. Instantaneous vertical velocity at 500 hPa in the vicinity of the mountain, from the  $h_0 = 1000$  m run, day 150, 19h.

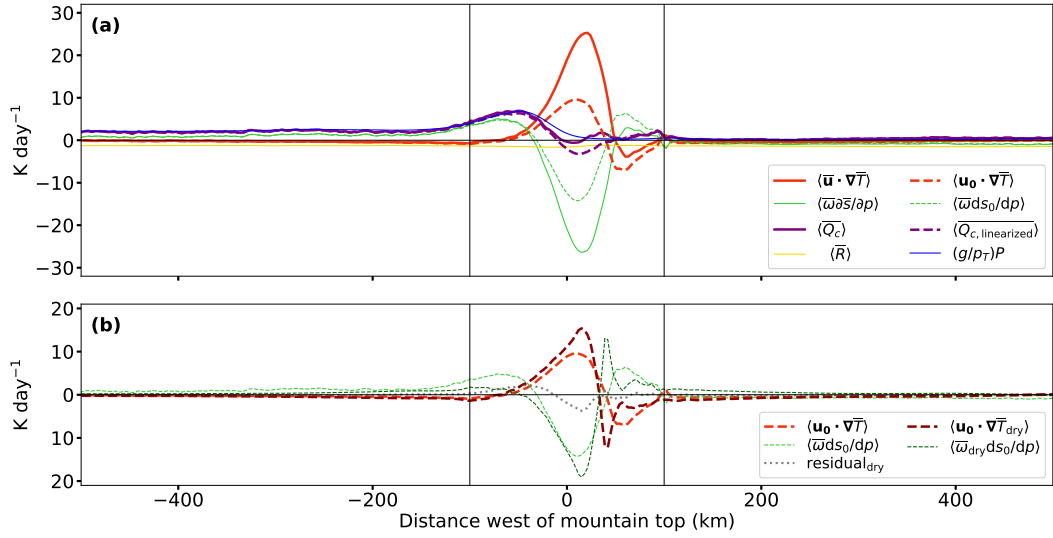


FIG. 6. Vertically averaged thermodynamic budget terms. Panel a shows ‘full’ (nonlinear) terms for the  $h_0 = 1000$  m control run, as well as their linearized version (obtained by fixing  $\mathbf{u}$  and  $s$  to their basic state values). The simulated precipitation rate is shown in blue for comparison. Panel b focuses on the linearized heat advection and adiabatic cooling terms, comparing the  $h_0 = 1000$  m control and  $L_v = 0$  runs. The vertical black lines show the extent of the mountain.

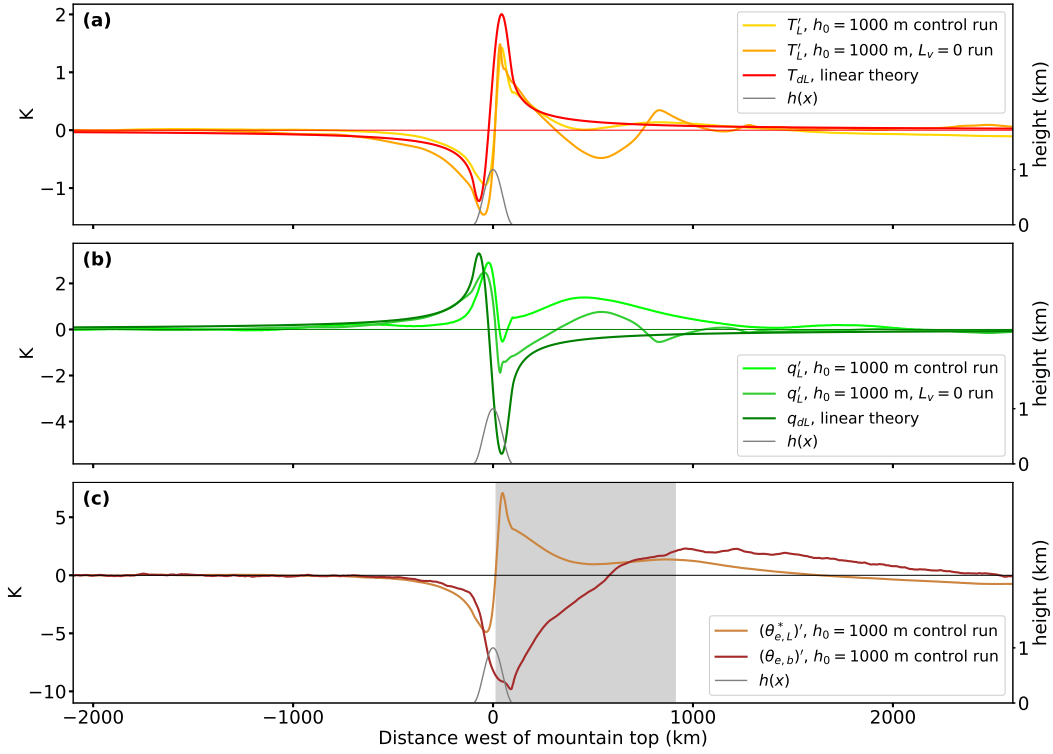


FIG. 7. Profiles of lower-tropospheric averaged temperature (a) and moisture (b) perturbations relative to 3000 km upstream in the  $h_0 = 1000$  m control and  $L_v = 0$  simulations, as well as perturbations computed from the linear theory ((8) and (12)). Panel c shows perturbations of lower-tropospheric averaged saturation equivalent potential temperature and boundary layer averaged equivalent potential temperature, in the  $h_0 = 1000$  m control run. Gray shading shows the convectively decoupled region where  $P_{1000} < 2 \text{ mm day}^{-1}$ .

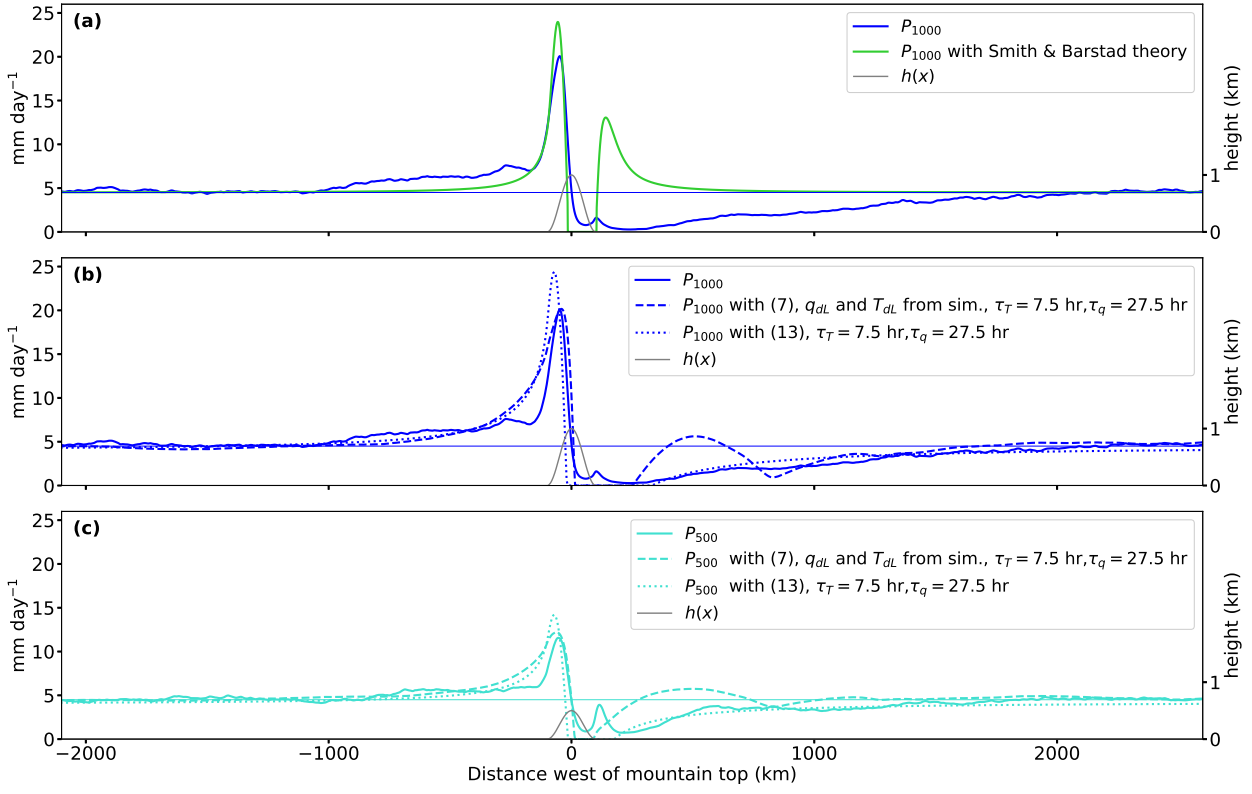


FIG. 8. Profiles of mean precipitation rates over 1000 m high (a and b) and 500 m high (c) mountains. Solid lines are simulated rates, dashed lines are computed from the nonlinear theory (7) with lower-tropospheric perturbations  $q_{dL}$  and  $T_{dL}$  diagnosed from simulations (see text), and dotted lines are profiles from the closed linear theory (13). The convective adjustment scales are taken from Ahmed et al. (2020) (a), then increased 2.5-fold (b and c). The thin horizontal lines show  $P_0$ .

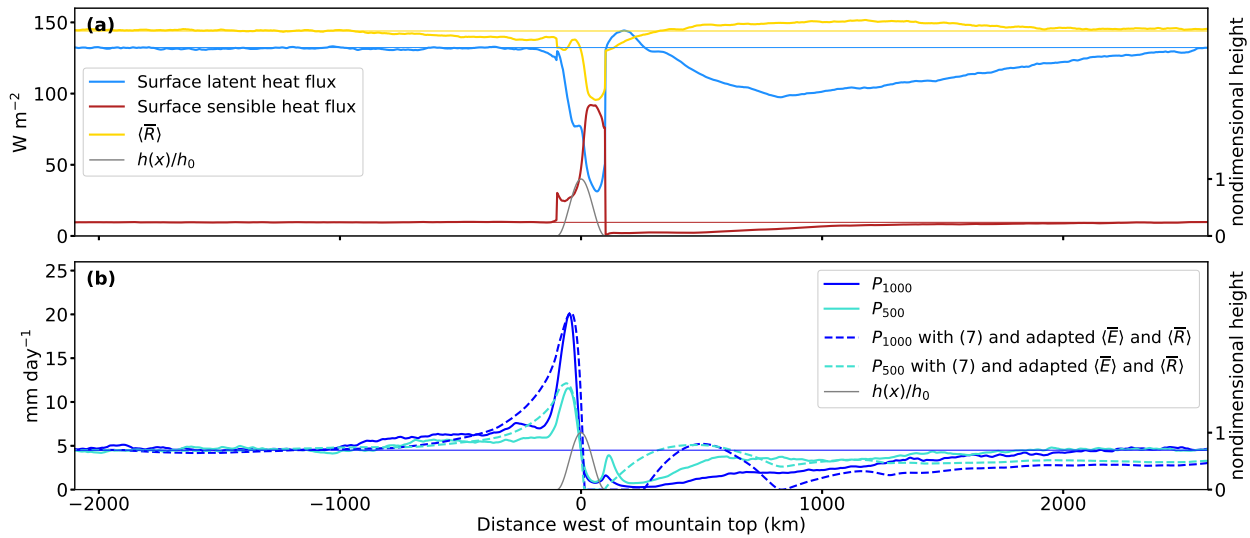


FIG. 9. (a) Time and meridionally averaged surface fluxes and radiative cooling from the  $h_0 = 1000$  m simulation. Thin horizontal lines indicate the upstream-averaged (between -2500 km and -3000 km) values. (b) As in Figure 8b,c, without solutions from (13), and where solutions from (7) take into account spatial variations in surface evaporation and radiative cooling. Compare the profiles between 1000 km and 2500 km downstream of the mountains.

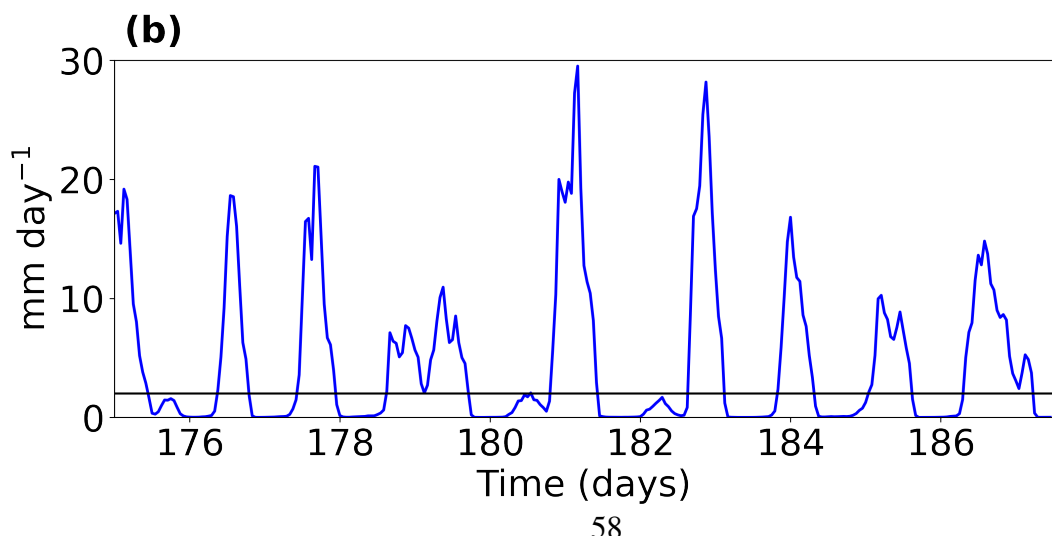
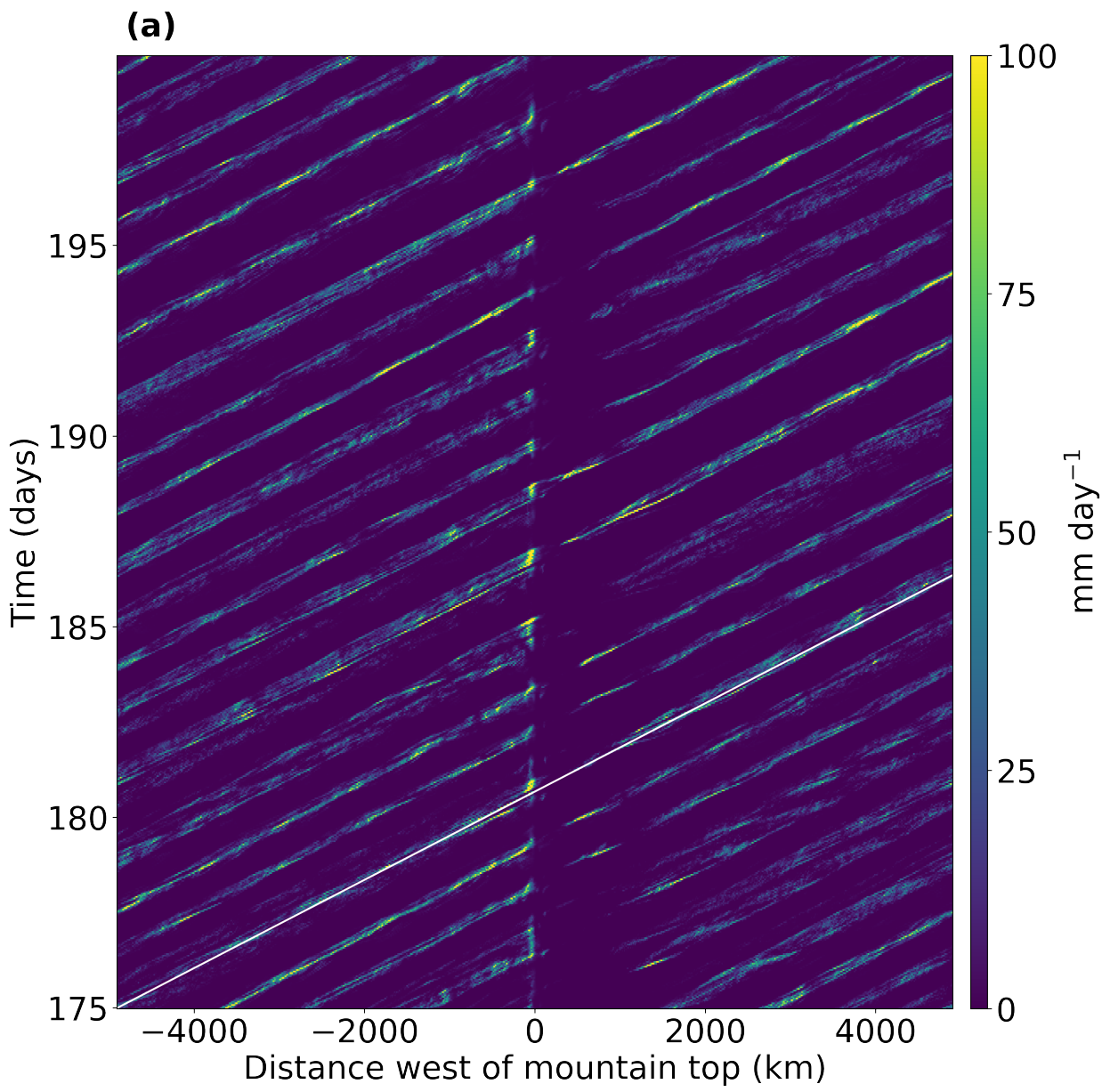


Fig. B1. (a) Hovmöller diagram of precipitation rate in the  $h_0 = 1000$  m run (in the  $x-t$  plane). An example characteristic line ( $L_{175\text{days}}$ ) is shown in white. (b) Precipitation averaged over characteristic lines. The  $x$ -axis shows the time at which a characteristic line starts, at  $x_0 = -4905$  km. The solid black line denotes the threshold defining a precipitating characteristic ( $2 \text{ mm day}^{-1}$ ).

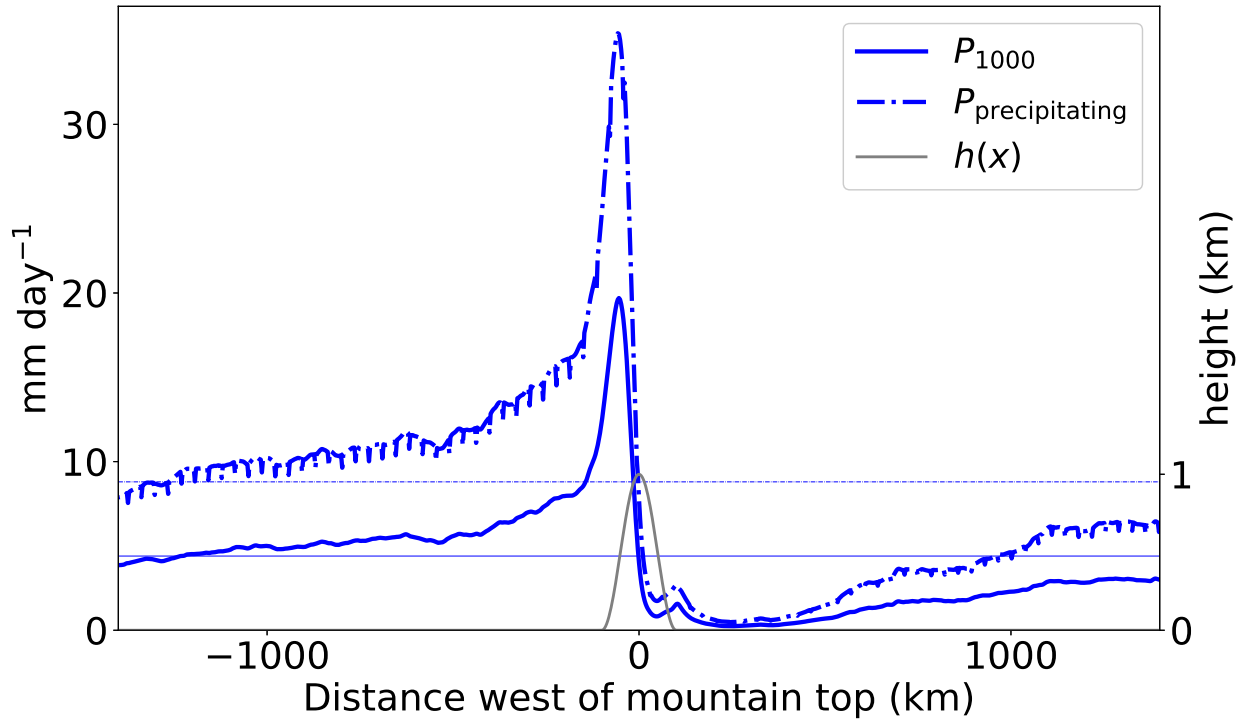


Fig. B2. Rain rate averaged over precipitating times only (see text), and all-time mean rain rate, for the  $h_0 = 1000$  m run.